Post-Print

E. Germaine, L. Mydlarski, L. Cortelezzi
Evolution of the Scalar Dissipation Rate Downstream of a Concentrated Line Source in Turbulent Channel Flow
Journal of Fluid Mechanics, Vol. 749, 2014, p. 227-274
doi:10.1017/jfm.2014.170

Evolution of the scalar dissipation rate downstream of a concentrated line source in turbulent channel flow

E. GERMAINE, L. MYDLARSKI† and L. CORTELEZZI
Department of Mechanical Engineering, McGill University, Montreal, Quebec, Canada

(Received ?; revised ?; accepted ?. - To be entered by editorial office)

The dissipation rate, ε_θ, of a passive scalar (temperature in air) emitted from a concentrated source into a fully developed high-aspect-ratio turbulent channel flow is studied. The goal of the present work is to investigate the return to isotropy of the scalar field when the scalar is injected in a highly anisotropic manner into an inhomogeneous turbulent flow at small scales. Both experiments and direct numerical simulations (DNSs) are used to study the downstream evolution of ε_θ for scalar fields generated by line sources located at the channel centreline ($y_s/h = 1.0$) and near the wall ($y_s/h = 0.17$). The temperature fluctuations and temperature derivatives were measured by means of a pair of parallel cold-wire thermometers in a flow at $Re_\tau = 520$. The DNSs were performed at $Re_\tau = 190$ using a spectral method to solve the continuity and Navier-Stokes equations, and a flux integral method (Germaine *et al.* 2013, 3DFLUX) for the advection-diffusion equation. The statistics of the scalar field computed from both experimental and numerical data were found to be in good agreement, with certain discrepancies that were attributable to the difference in the Reynolds number of the two flows. The return to isotropy of the small scales is never perfectly observed in any region of the channel for the downstream distances studied herein. However, a continuous decay of the small-scale anisotropy is observed for the scalar field generated by the centreline line source in both the experiments and DNSs. The scalar mixing is found to be more rapid in the near-wall region, where experimental results exhibit low levels of small-scale anisotropy. However, the DNSs, being performed at lower Re_τ, show that persistent anisotropy can also exist near the wall, independently of the downstream location. The role of the mean velocity gradient in the production of ε_θ (and therefore anisotropy) in the near-wall region is highlighted.

1. Introduction

The ability of turbulence to mix one or more scalars within a fluid is of particular relevance to a variety of engineering applications including combustion, pollution dispersion and heat transfer. Using premixed combustion as an example, reactions occur only if the fuel and oxidizer are sufficiently mixed at the molecular level prior to ignition. However, our comprehension and ability to predict turbulent mixing are limited because the fluid mechanics that governs turbulent mixing involve multi-scale phenomena for which the details are not yet fully understood.

The turbulent mixing process stretches and stirs the scalar field, which serves to increase the scalar gradients. The scalar fluctuations are then smoothed out by the molecular mixing that principally occurs at the smallest scales of the turbulence. The rate of destruction of the scalar variance is quantified by the scalar dissipation rate,

† Email address for correspondence: laurent.mydlarski@mcgill.ca

$\varepsilon_\theta (\equiv \alpha\langle(\partial\theta/\partial x_i)^2\rangle$. It is the only term in the scalar variance budget that must be non-zero in every turbulent flow. Consequently, ε_θ is omnipresent and of critical importance to the description of turbulent scalar fields. Furthermore, it is a quantity whose primary contributions derive from the smallest scales of the scalar field.

The predominant theory related to turbulent scalar mixing, Kolmogorov Obukhov Corrsin (KOC) theory, predicts that the small scales should be isotropic and independent of the large scales of a scalar field; the latter being anisotropic in most cases. However, it has been shown that departure from isotropy occurs at the small scales of the scalar field when its large scales are anisotropic, which puts KOC phenomenology into question (Warhaft 2000).

Investigations into the local isotropy of the scalar field (and, in particular, violations thereof) have been widely reported in the literature (e.g. Sreenivasan 1991). However, the large majority of these studies focussed on the evolution of a scalar field injected into a homogeneous and isotropic turbulent hydrodynamic field at large scales. Althought, the assumption of homogeneity considerably simplifies the analysis and yields interesting similarities between the scaling of the velocity and scalar fields when the injection occurs at large scales (Corrsin 1952; LaRue & Libby 1981; Ma & Warhaft 1986; Danaila *et al.* 2012). However, such a configuration is not representative of real flows, which are generally inhomogeneous and exhibit discrepancies between the scales of the velocity and scalar fields. Furthermore, only a small subset of the previous work has focussed on the dissipation rate of the scalar variance, even though ε_θ remains one of the less understood (yet most important) quantities within a turbulent flow.

The small-scale injection of a scalar by means of a point or line source in an inhomogeneous flow is of relevance to multiple engineering applications, including the transport of a plume emitted by a smokestack in the atmospheric boundary layer, or the mixing of chemical species injected into a combustion chamber. Given the importance of such applications, it is somewhat surprising that relatively few studies of turbulent scalar mixing resulting from small-scale injection and focusing on the scalar dissipation rate, ε_θ, have been undertaken. This fact motivates the research herein.

The main objective of the present work is to further investigate and understand the evolution of the scalar field when injected in a highly anisotropic manner at small scales in an inhomogeneous turbulent flow. In measuring the evolution of ε_θ downstream of the source, we aim to further our understanding of the details of the scalar mixing process, which will improve our effectiveness in predicting the phenomena that rely on this process. In many cases, local isotropy is invoked when estimating ε_θ. When the scalar is injected at small scales, such an assumption is clearly inaccurate near the source. Furthermore, though this assumption may increase in validity with increasing distance from the source, the rate at which it does so is an important factor. Therefore, particular attention will be paid to the evolution of the three different components of the scalar dissipation rate: $\varepsilon_{\theta_x} \equiv \alpha\langle(\partial\theta/\partial x)^2\rangle$, $\varepsilon_{\theta_y} \equiv \alpha\langle(\partial\theta/\partial y)^2\rangle$ and $\varepsilon_{\theta_z} \equiv \alpha\langle(\partial\theta/\partial z)^2\rangle$. We focus our attention on the relative contributions of ε_{θ_x}, ε_{θ_y} and ε_{θ_z} to ε_θ, and therefore on the evolution of this anisotropy. To this end, all three components of the scalar dissipation rate have been studied both, experimentally and by means of numerical simulations.

The remainder of this paper is organized as follows. The relevant literature is reviewed in §2. Then, the experimental apparatus and details of the numerical simulations are reported, respectively, in §3 and §4. Results are presented in §5, §6 and §7, comparing, as often as possible, the experimental and numerical results. The first of these three sections presents results pertaining to the velocity field. The second presents large-scale statistics (mean and root-mean-square (r.m.s.) temperatures), and compares them to the previous results of Lavertu & Mydlarski (2005) to validate the present measurements. The third

section, which comprise the vast majority of the results presented herein, reports in detail the evolution of the scalar dissipation rate and its three components at several locations. Lastly, conclusions are presented in §8.

2. Literature review

The theoretical foundation of (hydrodynamic) turbulence was proposed by Kolmogorov (1941). This work, commonly referred to as $K41$, introduces several concepts necessary to the description of the transport and dissipation of turbulent kinetic energy in a turbulent flow. As there is also significant interest in heat and mass transfer, Kolmogorov's arguments were extended by Obukhov (1949) and Corrsin (1951) to the transport of passive scalars, referred to as Kolmogorov Obukhov Corrsin (KOC) phenomenology. At sufficiently high Reynolds numbers ($Re = UL/\nu$, where U is an average fluid velocity, L is some characteristic length of the system, and ν is the kinematic viscosity of the fluid) and Péclet numbers ($Pe = UL/\alpha$ or UL/D, where α is the thermal diffusivity of the fluid and D the scalar (molecular) diffusivity of a chemical species in the fluid), it supposes that there is a decay of any large-scale anisotropy when smaller and smaller scales are considered, the scalar dissipative scales returning to a statistically isotropic state. The smallest hydrodynamic and scalar scales (η and η_θ, respectively) are related by the Prandtl number ($Pr = \nu/\alpha$) or Schmidt number ($Sc = \nu/D$). (Subsequently, in the interest of concision, we will assume the scalar under consideration is temperature in our discussions.) The relationship between η, η_θ and Pr depends on whether $Pr > 1$ or $Pr < 1$. Note that η_θ and η are of the same order of magnitude in the air flow studied herein, where $Pr = 0.7 \approx O(1)$. Therefore $\eta_\theta = \eta Pr^{-3/4}$ (Corrsin 1951), where $\eta = (\nu^3/\varepsilon)^{1/4}$ and where $\varepsilon \equiv 2\nu\langle s_{ij}s_{ij}\rangle$ is the dissipation rate of turbulent kinetic energy. ($s_{ij} \equiv \frac{1}{2}(\partial u_i/\partial x_j + \partial u_j/\partial x_i)$ is the fluctuating strain rate.)

The transport of a scalar quantity injected by a line source in a turbulent flow has been studied since the early experiments of Taylor (1935) and Uberoi & Corrsin (1952). Measurements taken downstream of a heated line source in homogeneous, isotropic turbulence were carried out by Warhaft (1984) and Stapountzis *et al.* (1986). The authors showed that, in isotropic turbulence, the development of the mean thermal wake can be divided into three stages corresponding to different times t: i) a molecular diffusive range ($t \ll \alpha/\langle v^2\rangle$, where $\langle v^2\rangle$ is the velocity variance in the transverse direction), in which the width of the mean temperature profile, σ_{mean}, increases as $\sqrt{t}$, ii) a turbulent convective range ($\alpha/\langle v^2\rangle \ll t \ll t_L$, where t_L is the Lagrangian integral time-scale) in which the growth of σ_{mean} is linear in time, and iii) a turbulent diffusive range ($t \gg t_L$) where σ_{mean} is proportional to $t^{(2-n)/2}$ (with $n \approx 1$ being the decay exponent of the velocity field). Subsequently, Karnik & Tavoularis (1989) investigated the evolution of a thermal plume in a homogeneous (but non-isotropic) turbulent shear flow. In contrast with grid turbulence, there is a continuous supply of kinetic energy from the mean shear to the turbulence, ensuring that the turbulence does not decay in this flow. The authors observed that the decay of the scalar fluctuations close to the source was not very different from that observed in isotropic turbulence. However, farther downstream, the mean shear affected the scalar statistics, imposing the effect of its large-scale anisotropy on the evolution of the scalar. Chung & Kyong (1989) also investigated the dispersion of a turbulent temperature field behind a line source in a homogeneous turbulent shear flow. Their goal was to provide experimental data for the assessment of third-order transport models. The mean and r.m.s. scalar profiles were found to exhibit nearly Gaussian distributions except for a minor degradation in the center region of the r.m.s. temperature profile. The evolution of second-order moments of scalar plumes, emitted from instanta-

neous and continuous area, line, and point sources, was modelled by Thomson (1996). Given that the flow under consideration was homogeneous, isotropic turbulence, he was also able to model the evolution of the scalar dissipation rate (via the scalar variance budget). Livescu *et al.* (2000) used Direct Numerical Simulations (DNSs) to study the development of the scalar plume produced by a line source in decaying homogeneous, isotropic turbulence. Their study focused on a statistical analysis of moments of different orders and confirmed the experimental results of Warhaft (1984).

Although previous work in homogeneous flows has drastically increased our understanding of the mixing of scalars emitted from sources at small scales, their applicability to engineering and natural flows remains somewhat limited given that almost all "real" flows (e.g. jets, boundary layers, duct flows) are inhomogeneous. Consequently, scalar dispersion within inhomogeneous flows has also been studied. To this end, Fackrell & Robins (1982) investigated the evolution of a thermal plume emitted from a point source in a turbulent boundary layer. The authors reported measurements of the variance, intermittency, peak concentration values, probability density function and spectra of the scalar field. They showed that most of the fluctuations are produced in the vicinity of the source, and that the maximum amplitude of the fluctuations is source-size dependent. Raupach & Legg (1983) studied the dispersion of a thermal plume emitted in a turbulent boundary layer from a line source. Their work was focused on testing first- and second-order closure models. To this end, they measured the dissipation rate of the temperature fluctuations by assuming local isotropy and using Taylor's hypothesis ($\varepsilon_{\theta iso} \approx (3\alpha/\langle U\rangle^2)\langle(\partial\theta/\partial t)^2\rangle$, where angular brackets represent averaged quantities). They reported that their measurements of ε_θ were 20% below its value inferred from the scalar variance budget. Paranthoën *et al.* (1988) studied the evolution of the temperature field downstream of a line source in a turbulent boundary layer and in a planar jet. They reported mean and r.m.s. profiles of the temperature field and proposed a rescaling scheme based on the temporal integral Lagrangian scale of the vertical velocity fluctuations. The scheme was shown to be efficient in rescaling the mean profiles, but not the r.m.s. profiles. Tong & Warhaft (1995) studied the dispersion and mixing of temperature fluctuations emitted in the self-similar region of an axisymmetric turbulent jet from two heated annular (ring) sources. The two sources were used to study the mixing of two independently introduced scalar fields. Their results contrasted with those obtained in grid turbulence (Warhaft 1984), where the mixing and dispersion was slower. The authors also showed that far downstream of the jet exit, the scalar field becomes independent of its method of introduction into the flow. Tong & Warhaft (1995) also examined the relationship between the integral-scale and dissipation-scale fluctuations in the far-field. Even though they reported that large- (θ^2) and small-scale ($\Delta\theta^2$) quantities become less coupled as the Reynolds number increases, conditional expectations of $\Delta\theta^2$ on θ exhibited a significant dependence of the former on the latter. Rosset *et al.* (2001) investigated the transport of temperature behind a line source in a turbulent jet and a turbulent boundary layer over a flat plate. The authors were particularly interested in the behavior of the scalar dissipation rate, ε_θ. Near the source, they observed a large anisotropy of the dissipative scales, which was explained by the high temperature gradient imposed by the source and by the flapping of the thermal wake. This anisotropy persisted downstream in the off-center region of the plume. However, in the central part of the plume, they reported a return to isotropy of the different components of ε_θ. Rosset *et al.* (2001) derived a model to estimate the return-to-isotropy time-scale and proposed arguments to explain this phenomenon. Nevertheless, they ultimately remarked that the details of the process remain to be understood.

One subset of inhomogeneous flows is of particular interest. Fully-developed, turbulent

duct flows, of circular or high-aspect-ratio cross-sections, are only inhomogeneous in one (the wall-normal) direction. Such a characteristic simplifies the analysis given that the inhomogeneity of the underlying velocity field is limited to one direction (as opposed to two or three). Brethouwer *et al.* (1999) used DNS to study the turbulent mixing of a passive scalar in fully-developed turbulent pipe flow. In their work, the scalar was released from a point source at the centreline of the pipe. They presented large-scale statistics, i.e., mean and r.m.s. concentration profiles, turbulent fluxes and probability density functions (PDFs) which, in this case, at the center of the flow, compared favorably to experimental data from grid-turbulence. The release of a scalar field from a line source in a turbulent channel flow has also been investigated in the experiments of Lavertu & Mydlarski (2005). The authors studied the evolution of the temperature field in turbulent channel flow. The line source was oriented in the spanwise (z) direction resulting in a thermal plume that was statistically two-dimensional. The authors reported large-scale statistics measured at different downstream locations in the scalar plume and for several wall-normal locations of the line source. They observed significant differences from the results in grid turbulence, which were attributed to the inhomogeneity of this flow in the wall-normal direction. Vrieling & Nieuwstadt (2003) and Costa-Patry & Mydlarski (2008) both studied the passive scalar mixing downstream of two line sources in fully-developed turbulent channel flow using DNSs and experiments, respectively. They showed that mean temperature values can be inferred from measurements downstream of a single source. However, the combined variance of two sources cannot be obtained by adding the variance of the individual sources. In contrast with Lavertu & Mydlarski (2005) and Costa-Patry & Mydlarski (2008), Bakosi *et al.* (2007) used probability density function methods and the IECM (interaction by exchange with the conditional mean) model to investigate the dispersion of a passive scalar released continuously from a concentrated source in a turbulent channel flow. One-point statistics of the scalar field were compared to the DNS data of Abe *et al.* (2004) and the experimental data of Lavertu & Mydlarski (2005). The width of the mean scalar profiles obtained with the IECM model were larger than those measured in the experiments at different downstream locations from the source. Boppana *et al.* (2012) performed Large-Eddy Simulations (LESs) of the dispersion of a scalar from a line source in a turbulent channel flow. They reported mean and r.m.s. profiles and PDFs of the scalar fluctuations. Their results were also compared to the experiments of Lavertu & Mydlarski (2005), which exhibited discrepancies for both the width and location of the profile's peak. Note that in contrast to Bakosi *et al.* (2007), the widths of the mean profile computed by Boppana *et al.* (2012) were smaller than those obtained from Lavertu's experiments. In addition, Boppana *et al.* (2012) observed a double peak in the r.m.s. profiles at downstream locations from the source ($x/h > 7.4$) that were not reported in the experiments. PDFs of both the LESs and experiments were in good agreement, except for the thermal fields generated by the centreline source. Lepore & Mydlarski (2011) studied the downstream evolution of a three-dimensional thermal plume in the turbulent channel flow released by a line source oriented in the wall-normal direction. They examined in detail the mean and fluctuating temperature fields at different locations in the thermal plume to highlight the differences between lateral and transverse dispersion. Lastly, Mydlarski *et al.* (2007) focused on the dissipation rate of a scalar field emitted from a line source in a turbulent channel flow. The authors confirmed that small-scale anisotropy is amplified at the interfaces between the plume and the ambient fluid. They reported that a large anisotropy occurs in regions of high turbulent intensity and their results showed that there may exist a competition between mechanisms that amplify and destroy anisotropy. However, ε_θ was not directly measured in this work, but was inferred from the scalar variance budget (given certain assumptions).

		Exp.	DNS
$\langle U \rangle_{y/h=1}$	[m/s]	5.3	-
$u_{rms_{y/h=1}}$	[m/s]	0.22	-
u_τ	[m/s]	0.26	-
$\eta_{y/h=1}$	[m]	0.28×10^{-3}	-
$Re(= \langle U \rangle_{y/h=1} h/\nu)$		10600	3600
$Re_\tau(= u_\tau h/\nu)$		520	190
$Re_\lambda(= u_{rms_{y/h=1}} \lambda_{y/h=1}/\nu)$		59	36
$y_s/h = 0.17$		$y_s^+ = 88$	$y_s^+ = 33$
$y_s/h = 1.0$		$y_s^+ = 520$	$y_s^+ = 190$

Table 1: Flow parameters. Properties of the flow considered in the experiments and numerical simulations, and source locations in terms of wall units. $\nu = 15 \times 10^{-6}\ m^2/s$.

In contrast to their work, the present work directly measures (all three components of) the scalar dissipation rate, using both experiments and numerical simulations.

3. Experimental apparatus

The experiments were conducted in the same open-circuit channel as the one used by Lavertu & Mydlarski (2005), Costa-Patry & Mydlarski (2008) and Lepore & Mydlarski (2011). The air flow is supplied by a Hudson Buffalo centrifugal blower powered by a 7.5 h.p. electric motor whose speed is monitored by an ABB ACS 600 controller. The air flow is filtered at the inlet of the motor to prevent particles (of diameter greater than 3 μm) from entering the channel. A flexible rubber coupling is used to join the blower output to the entrance of the flow conditioning section to minimize the transmission of any blower vibrations to the flow conditioning section. The latter consists of a wide-angle diffuser, a settling chamber and a contraction. After exiting the contraction, the flow that enters the channel is uniform and has a low-turbulence-intensity (0.25%).

The test section is 8 m long and has a large aspect ratio, i.e. the height of the channel in the spanwise (z) direction is large (1.1 m) compared to its width ($2h = 0.06$ m) in the wall-normal (y) direction, see figure 1. Consequently, the flow is statistically independent of z, away from the top and bottom walls of the channel. The development of the flow is accelerated by the addition of two 3 mm diameter cylindrical rods (located 3 mm from each wall, at the entrance of the test section) that trip the boundary layers that form on the test section walls. At the downstream end of the test section, where the measurements are recorded, the flow is fully-developed with a mean flow in the downstream (x) direction and zero mean wall-normal (V) and lateral (W) velocities. In the fully developed region, the flow is statistically stationary and one-dimensional with velocity statistics depending only on the wall-normal distance (y). Note that such a flow is statistically symmetric about the mid-plane. Lastly, 7.5 cm of honeycomb mesh (of 5 mm cell size) is used at the outlet to prevent perturbations from outside the channel from being communicated upstream, into the channel. The flow conditions are listed in table 1.

In the test section, the scalar (temperature) is injected into the flow by heating a fine line source. The latter is a 0.127 mm diameter Ni-Cr wire extended across the spanwise direction of the test section at wall-normal locations of $y_s/h = 1.0$ (channel centreline)

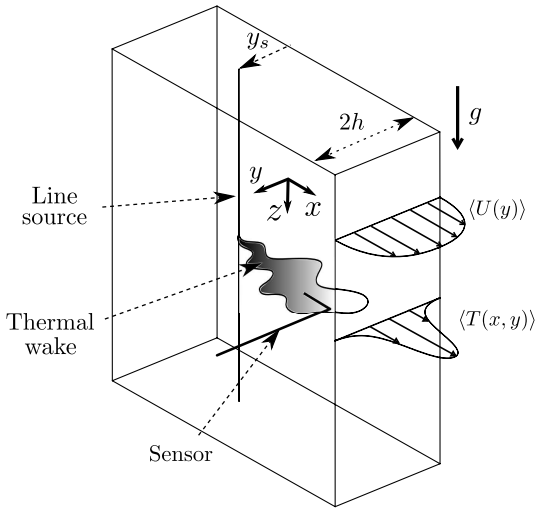

Figure 1: Schematic of the experiment. (Adapted from Lepore & Mydlarski (2011).)

.

and $y_s/h = 0.17$ (near-wall region). The wire was heated electrically by a DC power supply and the power consumption was continuously monitored so that the energy released into the flow remained equal to 45 W/m. See figure 1 for a schematic of the experiment.

The temperature fluctuations, θ, and their dissipation rate, ε_θ, were measured by means of cold-wire thermometry. The sensors were inserted into the channel from its outlet using a (915 mm-long) probe support (TSI-1155-36). The accurate positioning of the sensor in the wall-normal direction was ensured by means of a precision transversing mechanism driven by computer controlled stepper motor. The minimum step increment was 0.01 mm. The sensor consisted of two parallel 90%–platinum/10%–rhodium wires of 0.63 μm-diameter mounted on a TSI 1244 probe. Variations of the sensor temperature are linearly proportional to its electrical resistance (over small ranges) and are measured by a cold-wire thermometry circuit designed by Lemay & Benaïssa (2001). The output signals of the cold-wire thermometer were *i)* amplified and filtered by a Krohn-Hite 3384 8-pole filter, and *ii)* digitized using a 16 bit ($\pm 5V$) National Instruments PCI 6036E data acquisition card. The acquisition procedure was undertaken using LabVIEW virtual instruments. Depending on the wall-normal location of the probe, the sampling frequency (2.5 times the low-pass filter frequency) was in the range $[5-10]$ kHz and the sampling time was fixed at 200 s for each locations. The length-to-diameter ratio of the cold-wire sensors was approximately 800 (i.e. $l_{\text{wire}} \approx 0.5$ mm) and its frequency response was approximately 5 kHz when operated in a 5 m/s flow. Note that the temporal resolution of the wire was sufficient given that the Kolmogorov frequencies, $f_\eta = \langle U\rangle/(2\pi\eta)$, of the flow studied herein did not exceed 4 kHz. In addition, the (temporal resolution) correction proposed by Lemay & Benaïssa (2001) was applied to the acquired data. However, the effect of this correction was relatively small as it increased the estimate of the temperature dissipation by less than 1% when measured at the farthest downstream location and by 5% when measured at the location closest to the line source.

The scalar derivative $(\partial\theta/\partial x)$ in the downstream direction was estimated using Taylor's hypothesis in conjunction with the time derivative of temperature $(\partial\theta/\partial t)$. This measurement required only a single cold-wire, whereas, two wires were needed to estimate the derivatives $(\partial\theta/\partial y)$ and $(\partial\theta/\partial z)$ in the wall-normal and spanwise directions,

respectively. Zhou *et al.* (2003) investigated the effects of the separation between the two wires and found that the spectra of temperature derivatives are significantly affected by the electronic noise contamination from one wire to the other when the separation is smaller than 3η. In addition, they recommended the use of a correction method similar to that of Wyngaard (1969) when the wire separation was larger than 3η. As a consequence, we designed our sensors so that the separation between the two wires was nominally, 3η ($= 0.75$ mm), being slightly smaller than 3η at the channel centreline, and slightly larger near the wall, as η is a function of wall-normal position. This conclusion is furthermore supported by the works of Danaila *et al.* (2000), Anselmet *et al.* (1997) and Antonia & Mi (1993), who all agree that wire separations of 3η are optimal.

4. Numerical simulations

To complement the experiments described in §3 and provide further insight on the evolution of the scalar dissipation rate, we performed direct numerical simulations (DNSs) of a nearly identical problem. The fully developed turbulent flow can be assumed to be homogeneous in the spanwise and streamwise directions while the scalar field can be assumed homogeneous in the spanwise direction only. The scalar field presents a sharp gradient at the line source while the velocity gradients of the hydrodynamic field are smooth. However, since the temperature difference between the fluid in the plume and the incoming fluid are small, the hydrodynamic problem can be assumed to be one-way coupled with the adevection-diffusion problem. Therefore, we split the DNS in two parts: we first compute the solution to the hydrodynamic field and, subsequently, the solution to the advection-diffusion problem.

Spectral methods have become a standard tool to simulate fully developed turbulent channel flows because of their high-accuracy and kinetic energy conservation properties. We directly numerically simulate the time-evolution of the hydrodynamic flowfield by solving continuity and Navier-Stokes equations,

$$\frac{\partial U_i}{\partial x_i} = 0, \quad \frac{\partial U_i}{\partial t} + U_j \frac{\partial U_i}{\partial x_j} = -\frac{1}{\rho}\frac{\partial p}{\partial x_i} + \nu \frac{\partial^2 U_i}{\partial x_j \partial x_j}, \tag{4.1}$$

with periodic boundary conditions in the streamwise (x) and spanwise (z) directions, and no-penetration and no-slip conditions at the walls, see figure 1. The streamwise mean pressure gradient, which drives the mean flow in the x-direction, is adjusted dynamically to maintain a constant mass flux through the channel. To integrate the above equations, we use the spectral code named "Channelflow" (Gibson *et al.* 2008; Gibson 2010, licensed under the GNU GPL, `http://channelflow.org/`), which performes the time integration leveraging a third-order Runge-Kutta method.

Spectral methods, however, are not suitable for the simulation of a scalar field injected by means of a line source, i.e. a singularity, that introduces a sharp-gradient in the scalar field. In the presence of sharp-gradients, the convergence rate of spectral methods deteriorates to first-order because spurious oscillations develop in the vicinity of a line source and propagate in the flowfield (Gibbs phenomenon). Furthermore, spectral methods are not suited for solving non-periodic problems. (See, for example, Simens *et al.* 2009, for details.). Therefore, we solve the advection-diffusion equation

$$\frac{\partial T}{\partial t} + U_j \frac{\partial T}{\partial x_j} = \alpha \frac{\partial^2 T}{\partial x_j \partial x_j}, \tag{4.2}$$

with periodic boundary conditions in the spanwise (z) direction, inflow/outflow at the inlet/outlet of the channel, and adiabatic (no-flux) at the walls (see figure 1) using a

scheme we developed, named 3DFLUX (Germaine *et al.* 2013). 3DFLUX is a high-order, three-dimensional, conservative, monotonicity preserving numerical solver. It is nominally third-order in space and second-order in time. The line source used in the experiment is simulated using a string of constant-source nodes located on a straight line, oriented parallel to the z-axis.

In this two-step numerical approach, the solenoidal velocity field of the turbulent channel flow is precomputed by the Channelflow code and, subsequently, is passed as an input to the 3DFLUX code to solve the advection-diffusion equation. This passage, apparently trivial, is indeed very delicate because of the different velocity representations and grids used in the two codes. In Channelflow, the velocity field has a spectral representation with a resolution dictated by the number of Fourier and Chebyshev modes used. In 3DFLUX the computational domain is discretized with a number of non-overlapping control volumes or cells. The scalar field is discretized at the centre of each cell, whereas the components of the velocity field are stored at the centre of the faces of each cell (staggered grid). Therefore, the velocity field produced by Channelflow is passed to 3DFLUX by interpolating the spectral representation of the velocity field on each face of the 3DFLUX grid.

The interpolation of a divergence-free velocity field has been the subject of several publications in the last decade (see for example Balsara 2001; Li & Li 2004; Chamecki *et al.* 2008). The method proposed by Chamecki *et al.* (2008) is efficient only when the grids of the two different discretization methods are identical, and therefore not applicable herein. We devised our own method in which we first use a spectral (exact) interpolation to compute the value of the velocity components at nine points on each face, i.e. one at the center, four at the corners, and four at the mid-side of the edges of the faces. Then, we computed the value of each velocity component at the face of each cell by averaging the nine interpolated values. Finally, we applied a very small correction to the $u-$component of the velocity field to guarantee the exact divergence-free condition. Note that *i*) the choice of the $u-$component is arbitrary (it could have been the $w-$component), and *ii*) this correction has a minuscule impact on the velocity field, as it modifies the interpolated instantaneous values of the $u-$component by less than 0.01%.

The simulations of the velocity and scalar fields were both performed without turbulence models, by resolving the entire range of scales. The computational conditions are reported in table 2 for the (*i*) hydrodynamic field, and (*ii*) scalar field for two source locations ($y_s/h = 1.0$ and $y_s/h = 0.17$). These DNSs require that the computational domain be large enough to capture the integral scales and the spatial resolution be small enough to resolve, as accurately as possible, the dissipative scales. On the one hand, the large scales are correctly represented when the two-point correlations in the streamwise and spanwise directions are zero, respectively, at the half-length and half-height of the domain (Kawamura *et al.* 1998; Moser *et al.* 1999). The domain size selected herein is the same as in Kawamura *et al.* (1998), Moser *et al.* (1999) and Schwertfirm & Manhart (2007). The Kolmogorov (i.e. smallest) length scale should ideally be resolved. However, it has been claimed that this requirement is often too stringent. Moin & Mahesh (1998) noted that the smallest resolved length scale is required to be on the order of η but not equal to η. They further reported that very good agreement of *large-scale* statistics can be obtained between DNSs and experiments even though the Kolmogorov scales are not fully resolved in the simulation. Kawamura *et al.* (1998) validated the resolution of their simulations by showing substantial drop-offs in the one-dimensional energy spectra at high-wave numbers.

Traditionally, the goal of most experiments is to resolve all scales of size η or larger. This being said, recent work has taken advantage of the constantly increasing compu-

	velocity	scalar $y_s/h = 1.0$	scalar $y_s/h = 0.17$
$L_x \times L_y \times L_z$	$2\pi h \times 2h \times \pi h$	$2\pi h \times 2h \times \pi h$	$2\pi h \times 2h \times \pi h$
$L_x^+ \times L_y^+ \times L_z^+$	$1187 \times 378 \times 594$	$1187 \times 378 \times 594$	$1187 \times 378 \times 594$
$N_x \times N_y \times N_z$	$256 \times 193 \times 192$	$514 \times 195 \times 194$	$258 \times 390 \times 194$
$\Delta x^+, \Delta y^+, \Delta z^+$	$4.64, 0.025 - 3.1, 3.1$	$2.32, 1.96, 3.1$	$4.64, 0.98, 3.1$
$\Delta x^*, \Delta y^*, \Delta z^*$ at $y/h = 1.0$	$1.25, 0.83, 0.84$	–	–
$\Delta x^*, \Delta y^*, \Delta z^*$ at $y/h = 0.17$	$2.40, 0.88, 1.60$	–	–
$\Delta x^\bullet, \Delta y^\bullet, \Delta z^\bullet$ at $y/h = 1.0$	–	$0.50, 0.42, 0.66$	$0.99, 0.21, 0.66$
$\Delta x^\bullet, \Delta y^\bullet, \Delta z^\bullet$ at $y/h = 0.17$	–	$0.95, 0.80, 1.27$	$1.91, 0.40, 1.27$
t_{sam}^+	2770	665	665

Table 2: Details of the numerical grids for the computation of velocity, and scalar fields with two different source locations. The superscript "+" indicates the normalization by the viscous length (ν/u_τ) or time (ν/u_τ^2) scale, and the superscripts "$*$" and "$\bullet$" are used for the normalization by the Kolmogorov (η) and Corrsin (η_θ) length scales, respectively, estimated at $y/h = 1.0$ and 0.17 as specified.

tational power to simulate turbulent scalar mixing at spatial resolutions finer than η. For example, Schumacher *et al.* (2005) studied the fine structures of homogeneous and isotropic turbulent scalar mixing using high-resolution simulations (the grid spacing being smaller than η by a factor of two). They showed that when large fluctuations of ε exist, a spatial resolution based on η (defined using its average value) incorrectly predicted the small-scale statistics. Kozuka *et al.* (2009) and Galantucci & Quadrio (2010) both performed DNSs of turbulent scalar mixing in channel flows at high resolution. Galantucci & Quadrio (2010) carried out three DNSs at increasing spatial resolutions that they labelled Low, Medium and High. The Low resolution is comparable to the resolution of most wall-turbulence DNSs performed to date (with passive scalars) whereas, in the High resolution simulations, all cell sizes are consistently smaller than η_w, the averaged Kolmogorov length scale evaluated at the wall. The spatial resolution denoted Medium was midway between the two other resolutions. The authors reported several statistics pertaining to the rate of dissipation of the scalar field (mean, variance, and PDFs of ε_θ). They showed that the estimates of ε_θ can increase by 5% when using the High or Medium resolutions instead of the Low one. The resolutions used for the simulations presented herein (see table 2) are comparable to the Medium resolution used by Galantucci & Quadrio (2010). The accuracy of the chosen resolution as it pertains to the smallest scales in the flow will be subsequently confirmed when the normalized (one-dimensional) dissipation spectra for the simulations will be shown to be capable of reproducing the dissipative scales measured in the experiments.

To compute the hydrodynamic field, uniform meshes were used in the x- and z-directions whereas a non-uniform mesh (Chebyshev distribution) was adopted in the y-direction. As shown in table 2, two different grids were used to discretize the scalar field, depending on the source location. When the source was at the centreline, i.e. $y_s/h = 1.0$, a quasi-homogeneous grid was used given that the scalar plume did not interact with the walls (for the downstream locations studied herein). When the source was near the wall ($y_s/h = 0.17$), the grid resolution was halved in the y-direction to capture the smallest

wall-normal fluctuations of the scalar field that occur in the vicinity of the walls. The spatial resolution $(\Delta x, \Delta y, \Delta z)$ of the scalar field generated by the centreline source was, for either grid, smaller than or equal to the Corrsin scale. The spatial resolution of the scalar field generated by the near-wall source is, in the worst case, less than twice the Corrsin scale in the x-direction. However, note that Δy is always smaller than the Corrsin scale.

Lastly, to study the evolution of the scalar field at the farther downstream locations, we adopted a strategy that consisted in connecting several channels in series and computing the solution for the scalar field sequentially, i.e. the outflow of the first channel became the inflow of the second one, and so on. Note that the hydrodynamic field is the same in all channels because of its periodic boundary conditions. In this paper, we limited our computation to two channels, i.e. $(x/h)_{\max} = 2L_x/h$, where L_x is the length of one channel in the x-direction.

5. Results: Velocity field

To be consistent with Lavertu & Mydlarski (2005), the experiments were carried out (in the same experimental facility) at $Re_\tau = 520$. However, the simulations were performed at a lower Reynolds number ($Re_\tau = 190$) to resolve all scales while keeping the flow turbulent and the computational effort feasible. Mean velocity profiles in fully turbulent channel flow from both the experiments and DNSs are plotted in figures 2(a) and compared to the numerical results of Moser *et al.* (1999) ($Re_\tau = 180$ and 590) and Abe *et al.* (2001) ($Re_\tau = 180$ and 640). The experiments of Hussain & Reynolds (1975) ($Re_\tau = 640$) are also included for comparison. The mean velocity profile obtained from the present DNS is in very good agreement with those measured in flows at $Re_\tau = 180$. As noted by Kim *et al.* (1987), even if $Re_\tau = 180$ is a relatively low Reynolds number (for a turbulent flow), both linear and logarithmic regions exist and are distinct. Small differences are observed between the experiments and the DNSs. However, these differences can be attributed to the difference in Reynolds number of the flows – a conclusion that is confirmed by the good agreement between the present experimental results and the higher Reynolds number simulations of Moser *et al.* (1999) and Abe *et al.* (2001). These simulations also exhibit smaller values of u^+ for a given location y^+ in the logarithmic region.

The root mean square of the velocity fluctuations is plotted in figure 2(b). The data of Hussain & Reynolds (1975), Moser *et al.* (1999) and Abe *et al.* (2001) are once again reported for comparison, where available. The values of the three components (u^+_{rms}, v^+_{rms} and w^+_{rms}) increase with Re_τ and are consistent with differences in the Reynolds number between the present experiments ($Re_\tau = 520$), Moser *et al.* (1999) ($Re_\tau = 590$) and Abe *et al.* (2001) ($Re_\tau = 640$). Furthermore, the present DNS ($Re_\tau = 190$) agrees very well with the results of Moser *et al.* (1999) and Abe *et al.* (2001) (both with $Re_\tau = 180$). In short, figure 2(b) shows good agreement between the present and previous data obtained at similar Re_τ. (Note that the peak value of u^+_{rms} measured by Hussain & Reynolds (1975) is somewhat low compared the other results. This discrepancy may be justified by the difficulties in performing these early near-wall measurements). Finally note that original and interpolated velocity field are indistinguishable. Consequently only the former has been plotted.

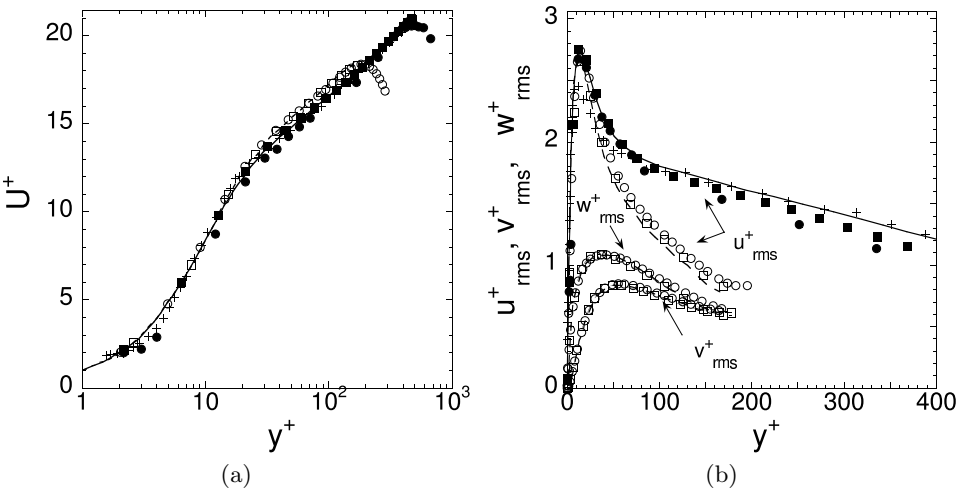

Figure 2: Velocity profiles in fully turbulent channel flow. Mean (a) and r.m.s. (b) velocity profiles (normalized by u_τ) from experiments ($Re_\tau = 520$, (•)), DNSs ($Re_\tau = 190$, (○)) and compared to the DNSs of Abe *et al.* (2001) ($Re_\tau = 180$, (- - -) and $Re_\tau = 640$, (—)) and Moser *et al.* (1999) ($Re_\tau = 180$, (□) and $Re_\tau = 590$, (■)), and the experiments of Hussain & Reynolds (1975) ($Re_\tau = 640$, (+)).

6. Results: Large-scale statistics of the scalar field

In this section, large-scale statistics of the scalar field from experiments and numerical simulations are analyzed and compared with those obtained in Lavertu & Mydlarski (2005). As the experiments were performed at a different Reynolds number than that of the numerical simulations, we normalized the downstream location (x/h) by the ratio $(u_{rms}/\langle U\rangle)^{-1}$ where u_{rms} and $\langle U\rangle$ are the r.m.s. and mean velocities measured at the centreline. Note that this normalization is equivalent to normalizing the flight time from the source by (an approximation of) the integral time scale ($t_L \approx h/u_{rms}$)

$$t/t_L = \frac{(x/\langle U\rangle)}{(\ell/u_{rms})} \approx \frac{(x/\langle U\rangle)}{(h/u_{rms})} = \frac{(x/h)}{(\langle U\rangle/u_{rms})}. \tag{6.1}$$

The mean temperature profiles at three downstream locations behind the line source ($t/t_L = 0.08,\ 0.2$ and 0.4) are shown in figures 3(a) and 3(b) for the $y_s/h = 1.0$ and 0.17 source locations, respectively. Given that mean temperature excesses ($\langle\Delta T\rangle \equiv \langle T\rangle - T_\infty$) can be difficult to measure accurately due to drift in the free-stream temperature, we used the technique proposed in Lepore & Mydlarski (2011), which consists of sequentially measuring the free-stream (i.e. ambient, room) temperatures at the same location, immediately after measuring the mean temperatures at a given (x, y) location in the thermal plume, to estimate the mean temperature excess based on the "instantaneous" free-stream temperature, which accounts for the aforementioned drifts in the free-stream temperature (as opposed to assuming T_∞ is the same for all measurements of $\langle T(x, y)\rangle$).

For the centreline source location ($y_s/h = 1.0$), very good agreement between the experiments and numerical simulations is observed, and the mean profiles are well approximated by Gaussian curve fits. (Gaussian fits are of interest for three reasons. Firstly, a Gaussian profile is the analytical solution to the advection-diffusion equation for the dispersion from a line or point source in a constant velocity and constant – laminar or

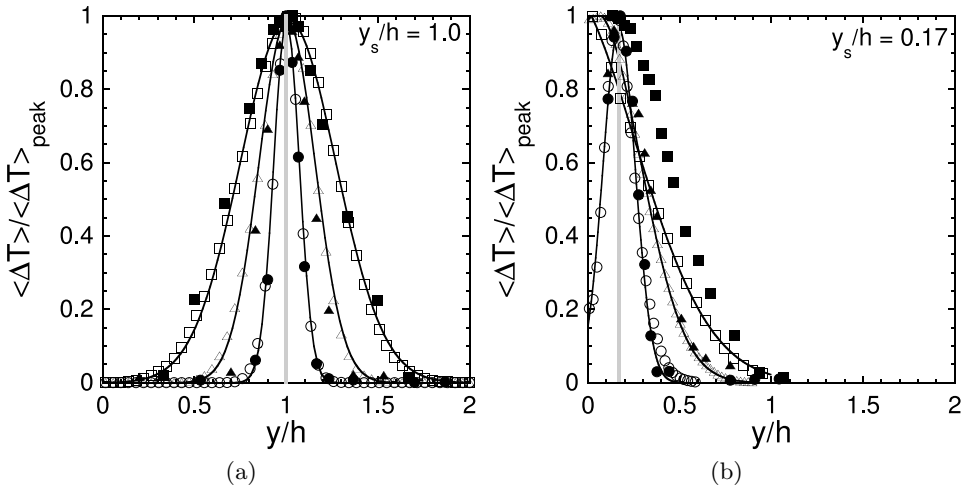

Figure 3: Non-dimensionalized mean temperature excess profiles for two line source locations, $y_s/h = 1.0$ (a) and $y_s/h = 0.17$ (b). Experiments (solid symbols) and DNSs (open symbols) are reported at several downstream locations: $t/t_L = 0.08$, (● and ○); $t/t_L = 0.2$, (▲ and △); $t/t_L = 0.4$, (■ and □), respectively. The vertical line indicates the transverse location of the source and the solid lines are the best fit Gaussian curve fits to the numerical data.

turbulent – diffusivity flow, which is approximately the case in the centre of the channel, and less so near the wall. Secondly, such fits assist in comparing with results that have been obtained in homogeneous turbulent flows, where Gaussian profiles have been observed. Thirdly, due to the least-square fitting process, fitting a curve to the data allows a more precise estimate of the standard deviation (or, alternatively, the half-width) of the plume by reducing error. We further note that the large-eddy simulations of Boppana *et al.* (2012), carried out at $Re_\tau = 520$ (i.e., the same value as the experiments herein), did not agree as well with the experiments of Lavertu & Mydlarski (2005) (that give very similar results to those herein – to be discussed shortly in the context of figures 5-8) and underestimated the plume width – see their figure 10(c). This presumably derives from their under-resolved transverse velocity fluctuations – they obtained values of $\langle v^2 \rangle$ at $y/h = 1$ that were 20% lower than the those obtained by Moser *et al.* (1999) at $Re_\tau = 590$ – see figure 5 in Boppana *et al.* (2012). Although a 20% underestimate of $\langle v^2 \rangle$ may not seem egregious, the observed good agreement between the present DNS and experiments implies that accurate estimates of $\langle v^2 \rangle$ are critical to reliably predicting the evolution of the plume. We furthermore remark that the PDF method simulations of Bakosi *et al.* (2007) overestimated the width of the mean profiles for a centreline source. However, the explanation in this case is less clear, especially given that they also under-resolved $\langle v^2 \rangle$ (see their figure 1(b)), as noted by Boppana *et al.* (2012).

Similarly, good agreement between the experimental and numerical mean temperature profiles is obtained for the near-wall line source ($y_s/h = 0.17$). However, for the farthest downstream distance considered herein ($t/t_L = 0.4$) the experimental mean temperature profile is wider than the numerical one. Far downstream of the source, the (two-dimensional) plume grows and becomes wider in the transverse direction. One edge of the plume is mixed with the cold flow contained in the central region of the channel, whereas the other edge comes in contact with the (nominally) adiabatic walls. Conse-

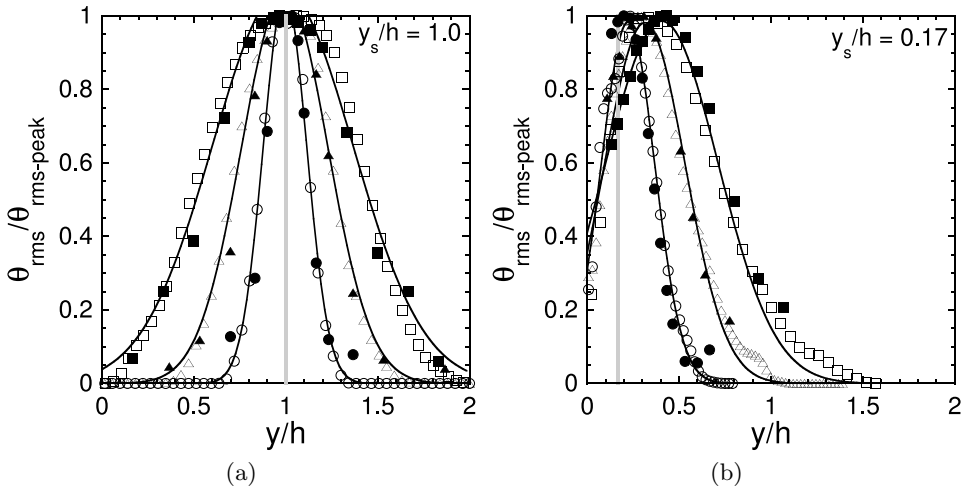

Figure 4: Non-dimensionalized r.m.s. temperature excess profiles for two line source locations, $y_s/h = 1.0$ (a) and $y_s/h = 0.17$ (b). Experiments (solid symbols) and DNSs (open symbols) are reported at several downstream locations: $t/t_L = 0.08$, (● and ○); $t/t_L = 0.2$, (▲ and △); $t/t_L = 0.4$, (■ and □), respectively. The vertical line indicates the transverse location of the source and the solid lines are the best fit Gaussian curve fits to the numerical data.

quently, the plume contains a hot region near the wall and a colder region away from the wall. The discrepancies observed for $t/t_L = 0.4$ in figure 3(b) are consistent with an energy loss (in the experiments) to the walls due to the latter not being perfectly adiabatic (because ΔT_{peak} is smaller than it should ideally be in the experiments due to the heat transfer from the plume to the wall). In dimensional terms, the peak mean excess temperature at $t/t_L = 0.4$ when $y_s/h = 0.17$, is less than 0.4°C, so even very minor energy losses to the channel wall, which is not perfectly adiabatic in reality, can have an effect. For the case of the centreline source, neither side of the plume comes in contact with the channel walls and the mean temperature profile remains symmetric about the line source location, in very good agreement with the numerical simulations. Like for the case of the centreline source, the large-eddy simulations of Boppana *et al.* (2012) were found to underestimate the width of the mean plume when $y_s/h = 0.17$ at all downstream locations – see their figure 10(b). This presumably derives from their under-resolved transverse velocity fluctuations, combined with the above-mentioned heat transfer to the wall in the experiments, which results in overly wide (normalized) plume widths farther downstream.

The simulations also exhibit a shift in the peak of the mean profile towards the region of lower velocity (i.e. towards the wall) when $y_s/h = 0.17$. A similar shift was reported in Karnik & Tavoularis (1989). At the wall, the simulated mean temperature profiles must all exhibit $\partial\langle T\rangle/\partial y|_{y=0} = 0$, consistent with the adiabatic boundary conditions imposed in our simulations. Experimental measurements in the range $0 < y/h < 0.1$ were, however, not possible due to interference of the probe with the wall.

The transverse profiles of the r.m.s. temperature fluctuations, θ_{rms}, normalized by their peak values, $\theta_{rms-peak}$, are reported in figures 4(a) and 4(b) respectively for $y_s/h = 1.0$ and 0.17 at three downstream locations: $t/t_L = 0.08,\ 0.2$ and 0.4. The experimental and numerical results collapse well for both line source locations, in addition to being well

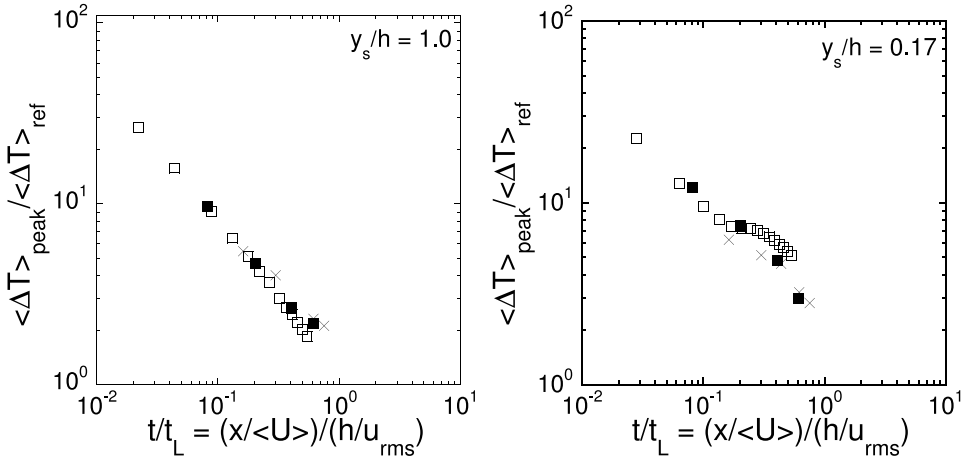

(a) (b)

Figure 5: Downstream evolution of the non-dimensionalized peak mean temperature for two line source locations: $y_s/h = 1.0$ (a) and $y_s/h = 0.17$ (b). Experiments (■), DNSs (□) and Lavertu & Mydlarski (2005) (×).

approximated by Gaussian curve fits. At $y_s/h = 1.0$, the peaks of the fluctuations remain behind the line source, as expected, by the underlying symmetry of this flow. However, for $y_s/h = 0.17$, a drift of the peak towards the centreline is clearly observed. Similar drifts have been reported in Fackrell & Robins (1982), Raupach & Legg (1983) and Lavertu & Mydlarski (2005). Also note the very good agreement between the experiments and simulations at $t/t_L = 0.4$ for the case of the near-wall source. The good collapse of the two r.m.s. profiles (when normalized by their peak value) reaffirms our hypothesis that the disagreement observed in figure 3(b) for the mean profiles at the same location arises from an underestimate of ΔT_{peak}. For a centreline source, the large-eddy simulations of Boppana *et al.* (2012) underestimate the plume width, similar to their results for the mean profile. For the case of the source at $y_s/h = 0.17$, the r.m.s. profiles of Boppana *et al.* (2012) are of a similar shape, but are offset and closer to the wall. Given that the r.m.s profiles are related to the mean profiles (i.e., the former can be predicted from the latter using gradient transport theory, for example), such a result is consistent with their mean profiles that are not as wide. Similar to the mean profiles, the simulations of Bakosi *et al.* (2007) overpredicted the width of the r.m.s.profiles.

The double-peaked r.m.s. profile in the vicinity of the source reported by Warhaft (1984) and Karnik & Tavoularis (1989) for homogeneous flows is also observed for the simulations (not shown). The double peak remains up to $t/t_L = 0.1$ ($x/h = 2.0$), after which the profile becomes single-peaked. Note that when $y_s/h = 0.17$ the double peak is not symmetric, as it must be for the centreline source case, with the near-wall peak having a lower magnitude. Lastly, note that experiments were not performed close enough to the line source to observe double-peaked θ_{rms} profiles.

Figures 5 and 6 respectively show the downstream decay of the peak of the mean and r.m.s. profiles normalized by a reference temperature

$$\langle \Delta T \rangle_{\text{ref}} = \frac{\int_0^{2h} \rho c_p \langle U \rangle \langle \Delta T \rangle \mathrm{d}y}{\int_0^{2h} \rho c_p \langle U \rangle \mathrm{d}y} = \frac{P_s}{\dot{m} c_p} \tag{6.2}$$

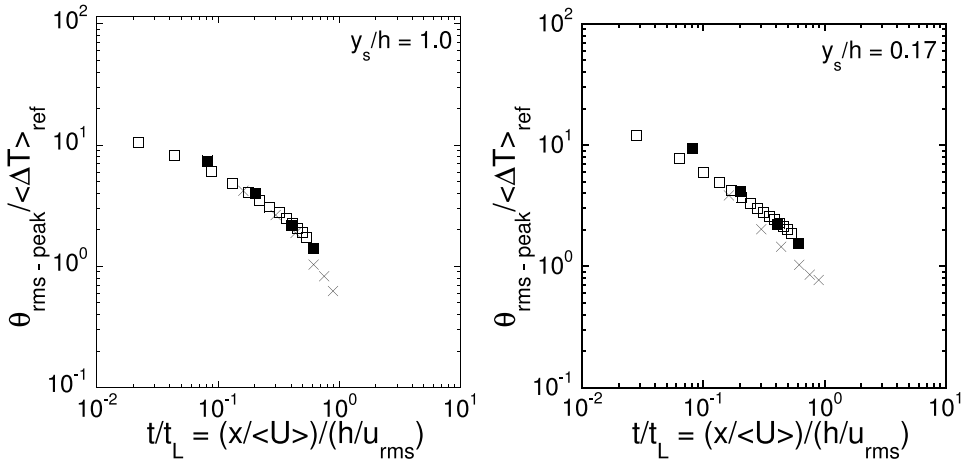

(a) (b)

Figure 6: Downstream evolution of the non-dimensionalized peak r.m.s. temperature for two line source locations: $y_s/h = 1.0$ (a) and $y_s/h = 0.17$ (b). Experiments (■), DNSs (□) and Lavertu & Mydlarski (2005) (×).

(see Incropera *et al.* 2007, p.495), where ρ and c_p are, respectively, the density and the specific heat at constant pressure of air, $\langle U\rangle = \langle U(y)\rangle$ is the mean velocity, P_s is the power of the line source, and $\dot{m}$ is the mass flow rate of air in the channel. Note that the above definition of $\langle\Delta T\rangle_{\rm ref}$ is different from that proposed by Rosset *et al.* (2001): $\langle\Delta T\rangle_{\rm ref} = (P_s/l_s)/(\rho c_p U_s d_s)$, where P_s/l_s is the electric power per length unit injected via the line source, U_s is the mean longitudinal velocity at the source location, and d_s is the source diameter. Such a reference temperature may not be appropriate if both the diameter of the source and the input power change. For instance, when d_s and P_s are each multiplied by two (assuming that the change of diameter has a negligible impact on the temperature profiles, which is reasonable for a very small diameter line source like those used herein), $\langle\Delta T\rangle_{\rm ref}$ should also be doubled to maintain a consistent normalization, which is not the case using their definition, due to the latter's dependence on d_s.

Figures 5 and 6 show good agreement between the numerical and experimental results – both the present ones and those of Lavertu & Mydlarski (2005). We note that the change in curvature observed in figure 5(b) is a consequence of the adiabatic walls. The downstream locations of the changes correspond to the locations at which the peak "encounters" the wall, and subsequently stops spreading on that side. Due to the adiabatic boundary conditions at the wall, the peak remains at $y = 0$ for all subsequent downstream locations. A similar change in curvature was observed for plumes emanating form a near-wall source in Boppana *et al.* (2012). Such a phenomenon, however, was absent in the case of the centreline source, as the downstream distances studied herein were not large enough for the plume to have grown sufficiently for its edges to interact with the channel walls.

The downstream evolution of the half-width of the mean and r.m.s. profiles (i.e. the widths of the profiles at the locations where they falls to 50% of their peak values) are plotted in figures 7 and 8, respectively, for the two source locations. The standard deviations σ are determined by best fitting a Gaussian curve to the data of figures 3 and 4. (Note that the standard deviation of the Gaussian profile is linearly related to its

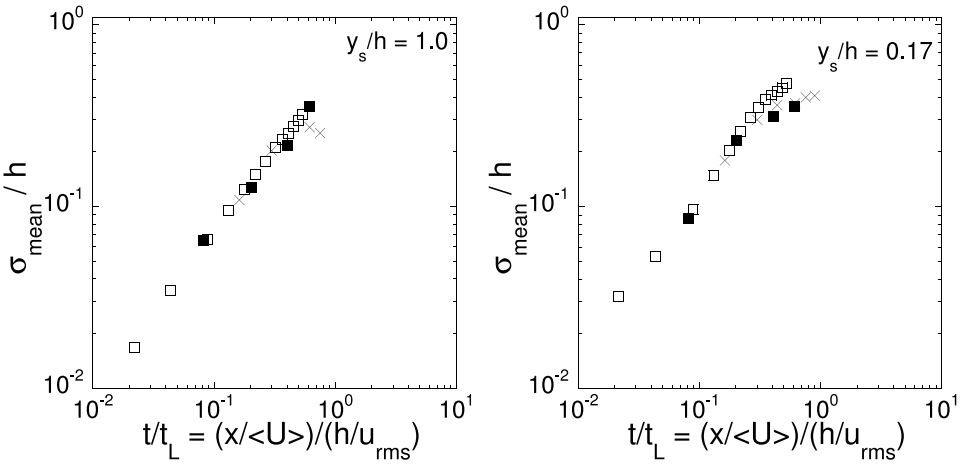

(a) (b)

Figure 7: Downstream evolution of the non-dimensionalized width of the mean temperature profiles for two line source locations: $y_s/h = 1.0$ (a) and $y_s/h = 0.17$ (b). Experiments (■), DNSs (□) and Lavertu & Mydlarski (2005) (×).

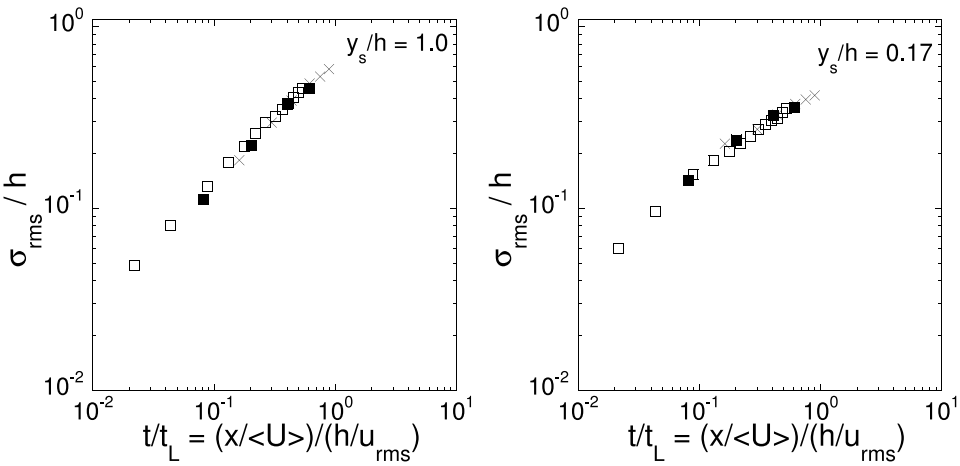

(a) (b)

Figure 8: Downstream evolution of the non-dimensionalized width of the r.m.s. temperature profiles for two line source locations: $y_s/h = 1.0$ (a) and $y_s/h = 0.17$ (b). Experiments (■), DNSs (□) and Lavertu & Mydlarski (2005) (×).

half-width.) Once again good agreement between experimental and numerical results is obtained. Note that in figure 7(b), the standard deviation of the numerical results tends to be larger than that of the experiments for the farthest downstream distance present herein, in contrast with the results of figure 3(b). This difference in fact derives from the fact that a Gaussian curve fit is not an especially accurate fit far downstream of the line source.

To complement the preceding analysis of large-scale statistics of the scalar field, we

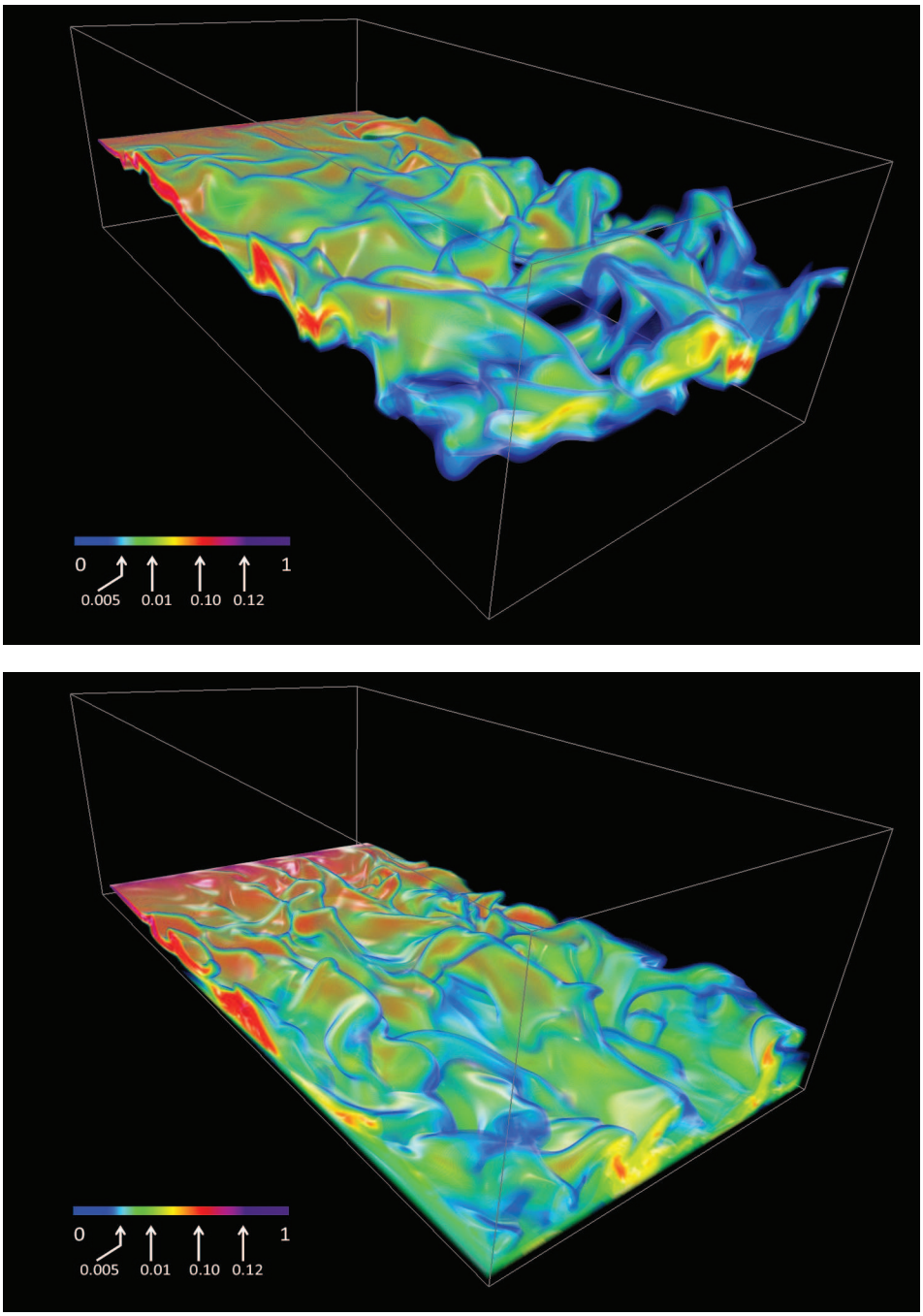

Figure 9: Instantaneous temperature fields generated (by DNS) downstream of line sources at two wall-normal locations: $y_s/h = 1.0$ (a) and $y_s/h = 0.17$ (b). $Re_\tau = 190$. $t^+ = 2770$ for the velocity field and $t^+ = 166$ for the scalar field (where, in the latter case, $t^+ = 0$ corresponds to the time at which the scalar is first injected into the flow). Note that the legend is non-linear in the non-dimensionalized temperature ($(T-T_\infty)/(T_{max}-T_\infty)$). Imagery produced by VAPOR (www.vapor.ucar.edu – see also Clyne & Rast (2005); Clyne *et al.* (2007))

.

plot in figure 9 the instantaneous temperature fields generated by our DNS downstream of both a centreline and near-wall line source. Note the "holes" in the temperature field for the plume emanating from the centreline source. Such holes are absent in the plume emanating from the near-wall source given the different nature of the mixing near the wall (including a reduced tendency of the plume to flap). The presence of the wall i) limits the plume's growth on one side, ii) is the cause of the flow's inhomogeneity (which is strongest near the wall), and iii) affects the mixing, as will be further discussed.

7. Results: Small-scale statistics of the scalar field

We now proceed to investigate the small-scale structure of the scalar field. Both experiments and numerical simulations are used in our analysis. We present statistics at various (downstream and transverse) locations behind the line source. The details of the measurement locations are specified in the figures.

7.1. *Spectra of θ, ε_θ and $\partial\theta/\partial x_\beta$*

We begin by plotting the one-dimensional longitudinal power spectra of the scalar fluctuations, $E_\theta(\kappa_1)$, where κ_1 is the longitudinal wavenumber. Results are presented for four downstream locations for each of the two line source locations studied herein, $y_s/h = 1.0$ and 0.17, in figures 10 and 11, respectively. The experimental results are obtained from time series, which provide Eulerian time spectra, $E_\theta(f)$. Eulerian spatial spectra, $E_\theta(\kappa_1)$, are obtained using Taylor's hypothesis $E_\theta(\kappa_1) = (\langle U\rangle/(2\pi))E_\theta(f)$, where $\kappa_1 = 2\pi f/\langle U\rangle$. Taylor's hypothesis is a reasonable approximation in most regions of the flow where $u_{rms}/\langle U\rangle < 10\%$. (See Sreenivasan *et al.* 1977; Prasad & Sreenivasan 1990, for example.) For consistency with the experiments, the numerical spectra were also computed from time series, so as not to introduce any artificial differences associated with the (small) errors induced by the inevitable use of Taylor's hypothesis in the experiments.

To compare experiments and simulations, the abscissa and ordinates were normalized by small scale quantities, i.e. $\varepsilon^{-3/4}\nu^{5/4}\varepsilon_{\theta_x}$ and $\eta = (\nu^3/\varepsilon)^{0.25}$. Note that the dissipation rate of the turbulent kinetic energy, ε, was determined using the assumption of local isotropy, i.e., $\varepsilon = 15\nu\int_0^\infty \kappa_1^2 E_u(\kappa_1)\mathrm{d}\kappa_1$, where E_u is the power spectrum of the longitudinal velocity fluctuations. Although the complete definition of ε can be computed in the DNS, the simulations calculated η using the above equation so that the results would be consistent with those obtained in the experiments (for which ε can only be estimated using the assumption of local isotropy). Near the centreline, this is an excellent assumption, however, very close to the wall, at locations outside of the range of experimental measurements undertaken in this work, it does introduce some error (Antonia *et al.* 1991). For example, at $y/h = 0.05$ (which corresponds to $y^+ \approx 10$ in the DNSs), the difference in estimates of the Kolmogorov microscale is ~ 2. ε_{θ_x} was determined from its definition $(-\alpha/\langle U\rangle^2)\langle(\partial\theta/\partial t)^2\rangle$ and also invoking Taylor's hypothesis.

Figures 10 and 11 show very good agreement between the experimental and numerical results at large κ_1, independent of the line source location. However, some differences exist at small κ_1 for the spectra measured downstream of the centreline line source (see figure 10) due to the difference in Reynolds numbers between the experimental and numerical flows. (Given that the normalization is based on small-scale quantities, one cannot expect spectra of the two flows at different Reynolds number to be the same at large scales.) Note that the turbulence intensity (and therefore local Reynolds number) is higher in the near-wall region and, hence, the mixing more effective (Lavertu & Mydlarski 2005). As a consequence, the agreement between experimental and numerical results at small

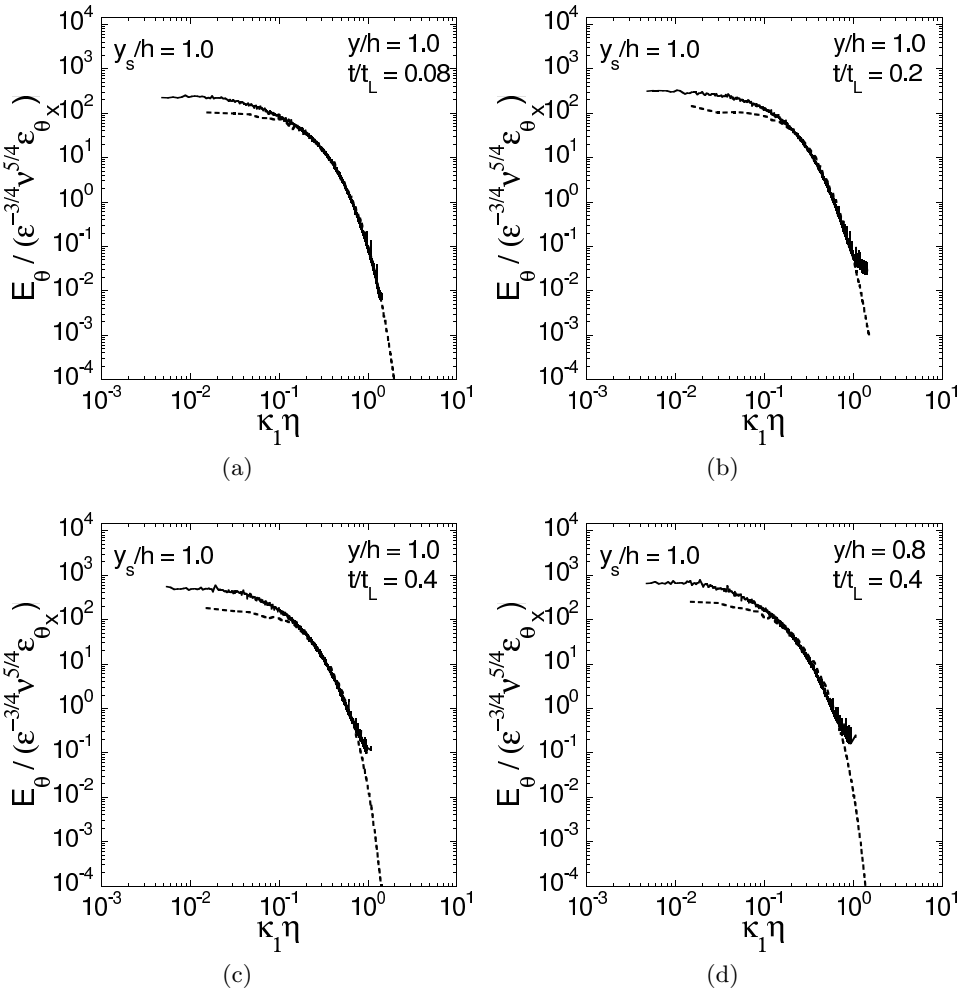

Figure 10: One-dimensional longitudinal spectra of the temperature fluctuations for $y_s/h = 1.0$ at three downstream locations: $t/t_L = 0.08$ (a), $t/t_L = 0.2$ (b) and $t/t_L = 0.4$ (c, d) and at two wall-normal locations: $y/h = 1.0$ (a-c) and $y/h = 0.8$ (d). Results from experiments (solid line) and DNSs (dashed line) are reported.

to medium κ_1 is better for the scalar field generated by the near-wall source (figure 11) than that for the centreline source (figure 10).

One-dimensional streamwise dissipation spectra, i.e. $\kappa_1^2 E_\theta(\kappa_1)$, for thermal fields originating from line sources located at $y_s/h = 1.0$ and $y_s/h = 0.17$ are plotted in figures 12 and 13, respectively. The experiments and DNSs are in good agreement at all measurement locations for both line source locations. Note that the normalization used in these figures implies that the area under each curve is equal to the Prandtl number ($Pr = 0.7$). As previously noted, these results serve to confirm that the resolution of our DNSs is sufficient to *i*) accurately resolve the contributions to ε_θ, and *ii*) reproduce the range of length scales measured in the experiments.

The dissipation spectra are generally found to peak at $\kappa_1\eta \approx 0.2$ showing that most of the dissipation occurs at length scales five times larger than η, consistent with the finding

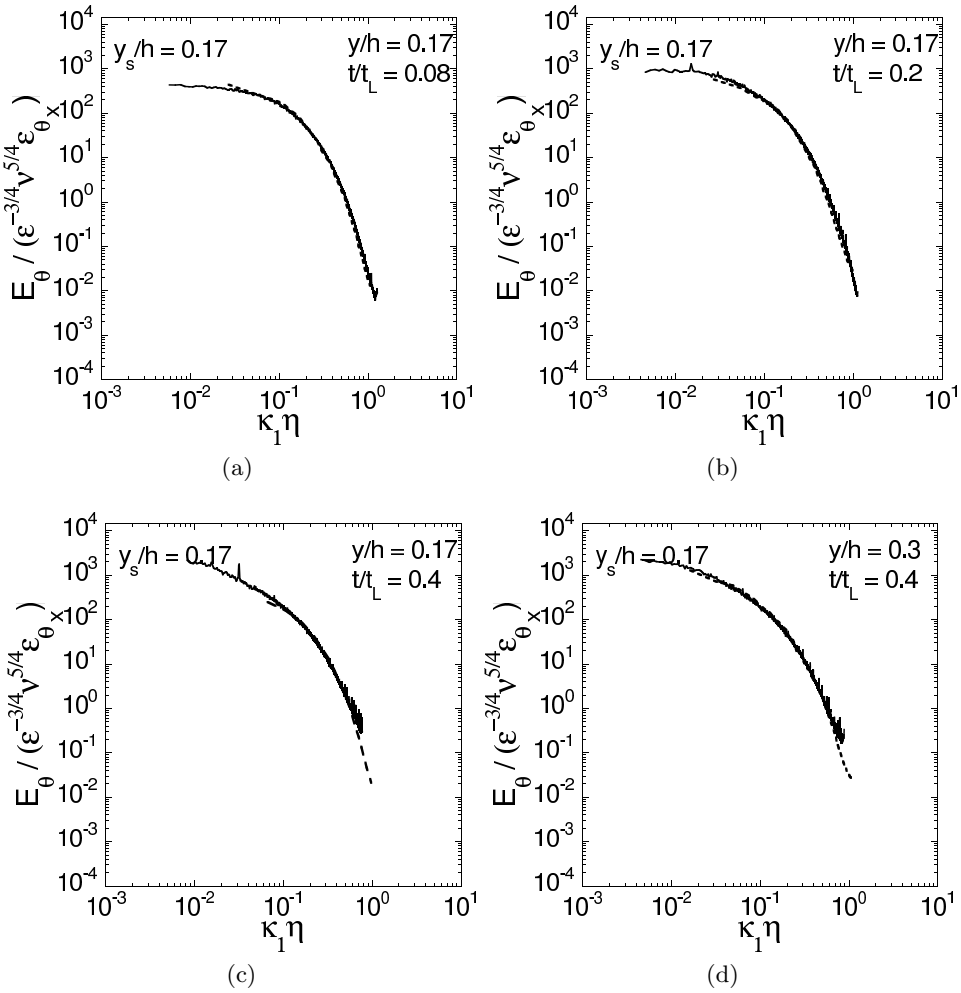

Figure 11: One-dimensional longitudinal spectra of the temperature fluctuations for $y_s/h = 0.17$ at three downstream locations: $t/t_L = 0.08$ (a), $t/t_L = 0.2$ (b) and $t/t_L = 0.4$ (c, d) and at two wall-normal locations: $y/h = 0.17$ (a-c) and $y/h = 0.3$ (d). Results from experiments (solid line) and DNSs (dashed line) are reported.

of Kozuka *et al.* (2009). However, a slight drift of the peak locations with increasing downstream distance from larger to smaller κ_1 for the centreline source is observed. (The peak occurs at $\kappa_1\eta = 0.26,\ 0.21$ and 0.17 for $t/t_L = 0.08,\ 0.2$ and 0.4, respectively.) Such a trend is not observed downstream of the near-wall sources. This may be attributed to the increased mixing that occurs near the wall (Lavertu & Mydlarski 2005).

We proceed to analyze the components of the dissipation spectra by examining one-dimensional spectra of the temperature derivative $\partial\theta/\partial\beta$, where $\partial\theta/\partial\beta$ is the β-derivative of the scalar fluctuations ($\beta = x,\ y$ or z). To this end, figures 14 and 15 plot spectra of the streamwise (x), wall-normal (y) and spanwise (z) components of the fluctuating temperature gradient, i.e. $E_{\partial\theta/\partial\beta}$. $E_{\partial\theta/\partial x}$ was measured by assuming Taylor's hypothesis, whereas the other two were measured using a second-order finite difference approximation. Note that the streamwise (one-dimensional) spectrum tends towards zero at large

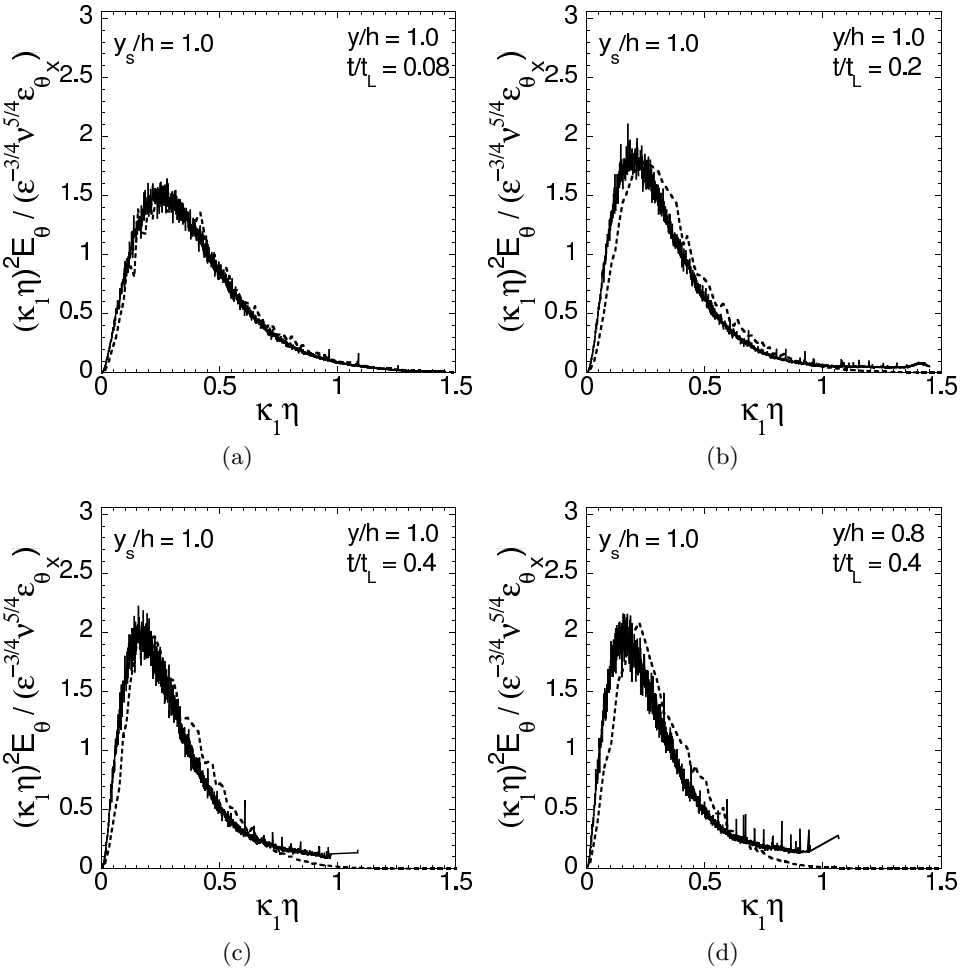

Figure 12: One-dimensional longitudinal dissipation spectra of the temperature fluctuations for $y_s/h = 1.0$ at three downstream locations: $t/t_L = 0.08$ (a), $t/t_L = 0.2$ (b) and $t/t_L = 0.4$ (c, d) and at two wall-normal locations: $y/h = 1.0$ (a-c) and $y/h = 0.8$ (d). Results from experiments (solid line) and DNSs (dashed line) are reported.

scales, which differs from the two other spectra that are subject to aliasing and have a finite value at zero wavenumber (Van Atta 1991). This difference is therefore *not* dynamical and thus not indicative of a lack of local isotropy. Note that the spectra were normalized by $\varepsilon_\theta \eta/\nu$, where $\varepsilon_\theta = \varepsilon_{\theta_x} + \varepsilon_{\theta_y} + \varepsilon_{\theta_z}$ and where η was computed using the assumption of local isotropy.

The present spectra are similar to those reported by Van Atta (1991) and Thoroddsen & Van Atta (1996), who studied scalar dissipation in decaying stably stratified grid turbulence. The authors showed that the large and small scales are anisotropic near the grid but become strongly anisotropic farther downstream in their stratified flow. Interestingly, they noticed that all scales develop anisotropies at about the same rate.

In the present research, the scalar is injected in a highly anisotropic manner that produces sharp gradients in the y-direction in the vicinity of the source. This anisotropy is shown in both figures 14(a) and 15(a) where $\varepsilon_{\theta_y} > \varepsilon_{\theta_z}$. However, the gap between ε_{θ_y}

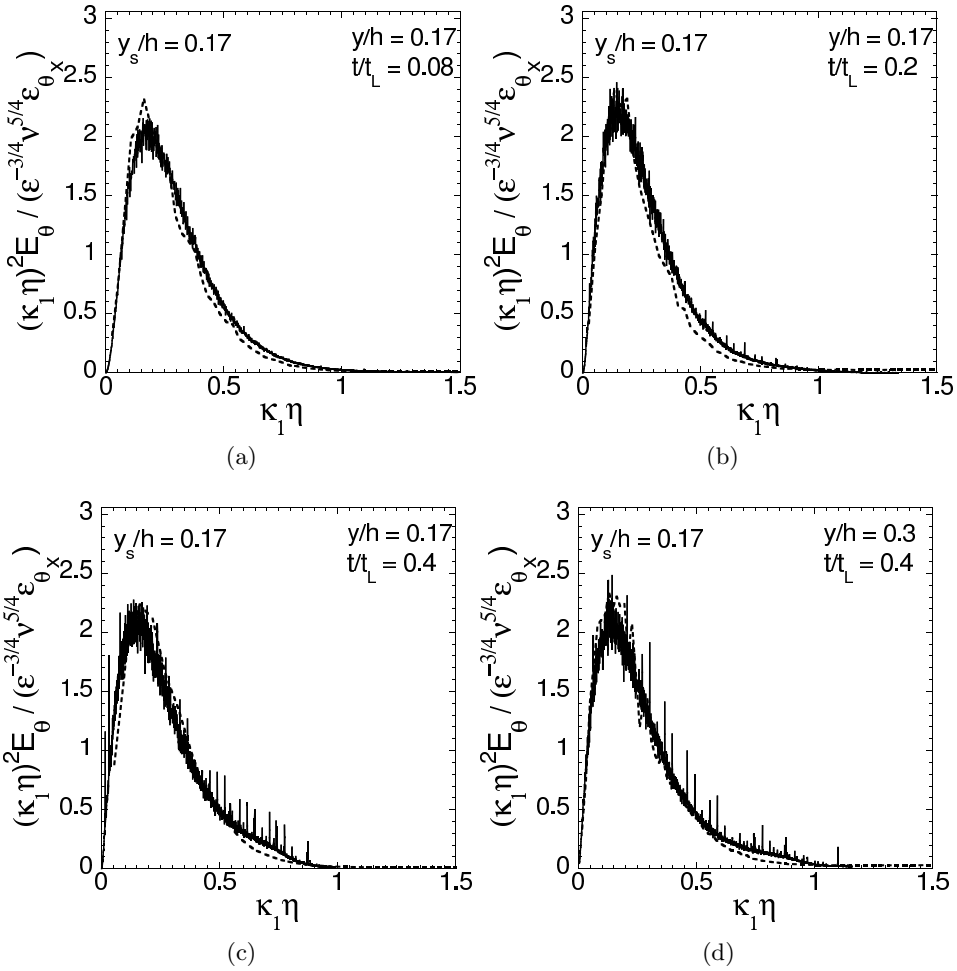

Figure 13: One-dimensional longitudinal dissipation spectra of the temperature fluctuations for $y_s/h = 0.17$ at three downstream locations: $t/t_L = 0.08$ (a), $t/t_L = 0.2$ (b) and $t/t_L = 0.4$ (c, d) and at two wall-normal locations: $y/h = 0.17$ (a-c), $y/h = 0.3$ (d) $y/h = 0.6$ (f). Results from experiments (solid line) and DNSs (dashed line) are reported.

and ε_{θ_z} diminishes considerably with increasing downstream distance. Ultimately, the experimentally measured spectra of ε_{θ_y} and ε_{θ_z} at $t/t_L = 0.4$ (figure 14(c)) are almost indistinguishable, which shows a clear tendency of the scalar dissipation rate towards isotropy. It is also interesting to note that the collapse between the spectra of ε_{θ_y} and ε_{θ_z} appears even sooner when the source is in the near-wall region (i.e. $t/t_L = 0.2$ as shown in 15(b)). This can again be attributed to the higher turbulence intensity (and therefore better mixing) that occurs in the near-wall region.

Figures 14 and 15 exhibit good agreement between the experiments and DNSs at large wavenumbers, especially for the centreline line source. Furthermore, a similar good agreement is also reported at small wavenumbers when the line source is located at the centreline, which reinforces the validity of the results presented herein. However, discrepancies exist at small wavenumbers when the line source is in the near-wall region. The numerical results exhibit a persistent anisotropy between ε_{θ_y} and ε_{θ_z} when $y_s/h =$

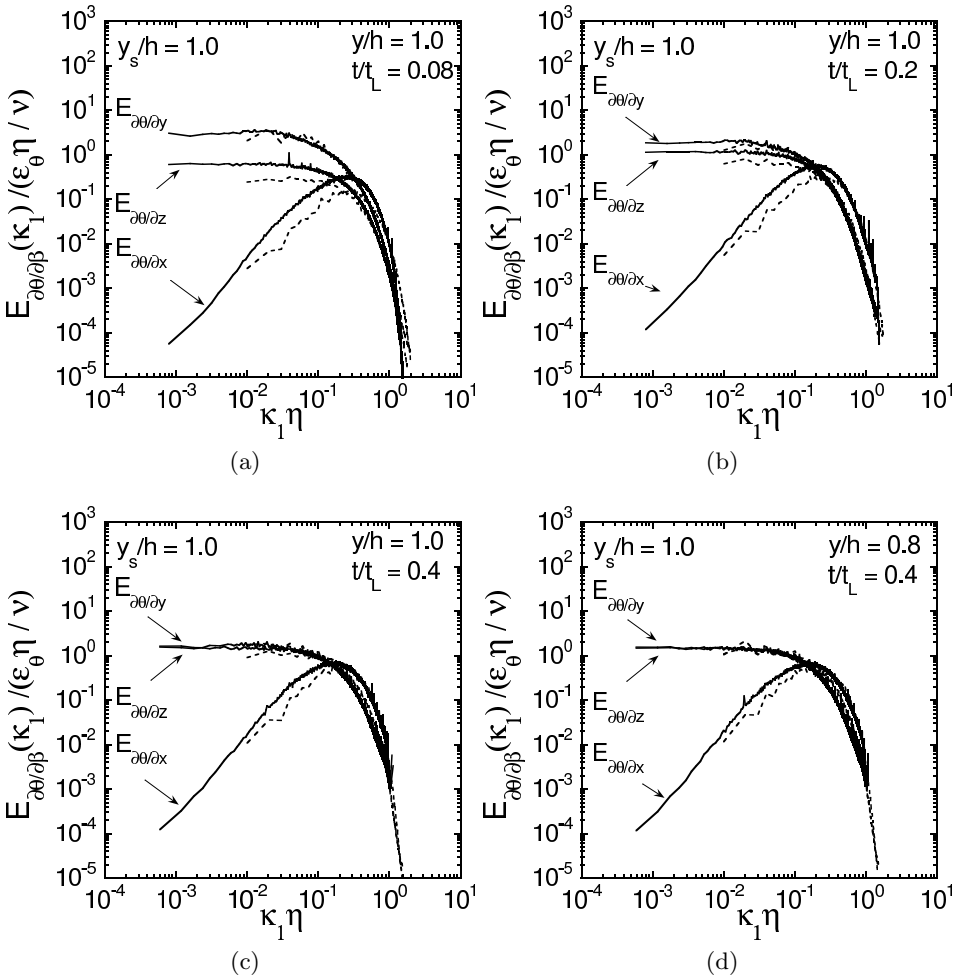

Figure 14: One-dimensional spectra of the temperature derivatives ($\partial\theta/\partial\beta$ where $\beta = x, y$ or z) for $y_s/h = 1.0$ at three downstream locations: $t/t_L = 0.08$ (a), $t/t_L = 0.20$ (b) and $t/t_L = 0.40$ (c-d), and at two wall-normal locations: $y/h = 1.0$ (a-c) and $y/h = 0.8$ (d). Results from experiments (solid line) and DNSs (dashed line) are reported.

0.17. These discrepancies are related to the production of ε_θ by mean velocity gradients, which occurs away from the centreline, near the wall. This effect will be discussed in more detail further on in this section. The reader is also referred to Gonzalez (2000), which describes the effects of mean velocity and temperature gradients on the isotropy of ε_θ in detail.

7.2. *PDFs of $\partial\theta/\partial x_\beta$ and ε_θ*

The PDFs of the temperature derivatives are plotted in figures 16 and 17 for line sources located at $y_s/h = 1.0$ and 0.17, respectively. The PDFs of the three components are quite different from each other near the source and become similar at the farthest downstream distance, where they develop quasi-exponential tails. Close to the source, figure 16(a) shows three peaks in the simulated PDF of the wall-normal temperature derivative, $P(\partial\theta/\partial y)$, whereas the PDFs of the other two derivatives are unimodal. These

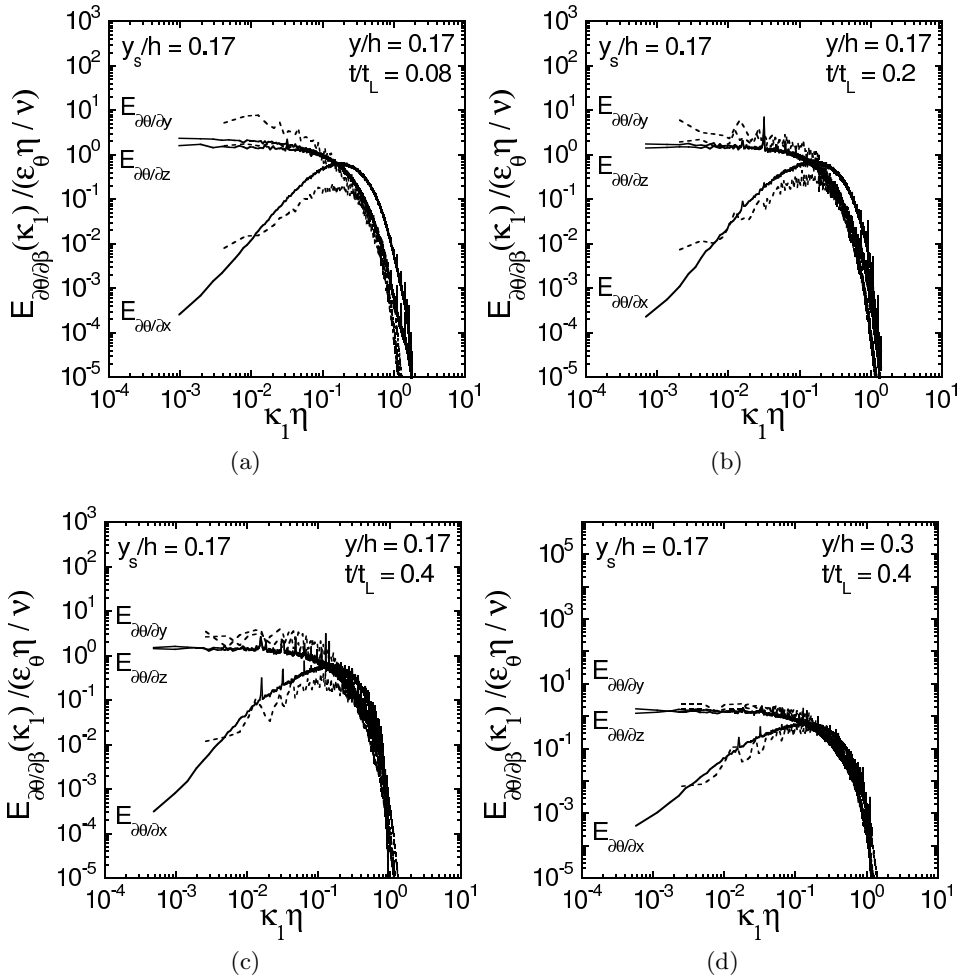

Figure 15: One-dimensional spectra of the temperature derivatives ($\partial\theta/\partial\beta$ where $\beta = x, y$ or z) for $y_s/h = 0.17$ at three downstream locations: $t/t_L = 0.08$ (a), $t/t_L = 0.20$ (b) and $t/t_L = 0.40$ (c, d), and at two wall-normal locations: $y/h = 0.17$ (a-c) and $y/h = 0.3$ (d). Results from experiments (solid line) and DNSs (dashed line) are reported.

triple peaks are due to the nature of the temperature field immediately downstream of the source. For very small t/t_L, the plume is a top-hat profile and thus we expect the PDF to be given by two delta functions where the two peaks are nominally at $\pm\left(T_{wire} - T_\infty\right)/(d_s/2)$, where d_s is the source diameter. However, slightly farther away from the source, after some mixing has occurred, the principal peak (or mode) starts to emerge while the other two initial peaks recede. Even farther away from the source, the peaks from the initial top-hat profile disappear and the PDF develops exponential tails, in this case, characteristic of a well-mixed scalar. In the near-wall region, the mixing being better, the initial peaks disappear very quickly and the initial trimodal PDF is not observed for the measurement locations considered herein. For a similar reason, the experimentally measured $P(\partial\theta/\partial y)$ (being at a higher Reynolds number) is also unimodal although of a shape that would be consistent with a trimodal PDF farther upstream.

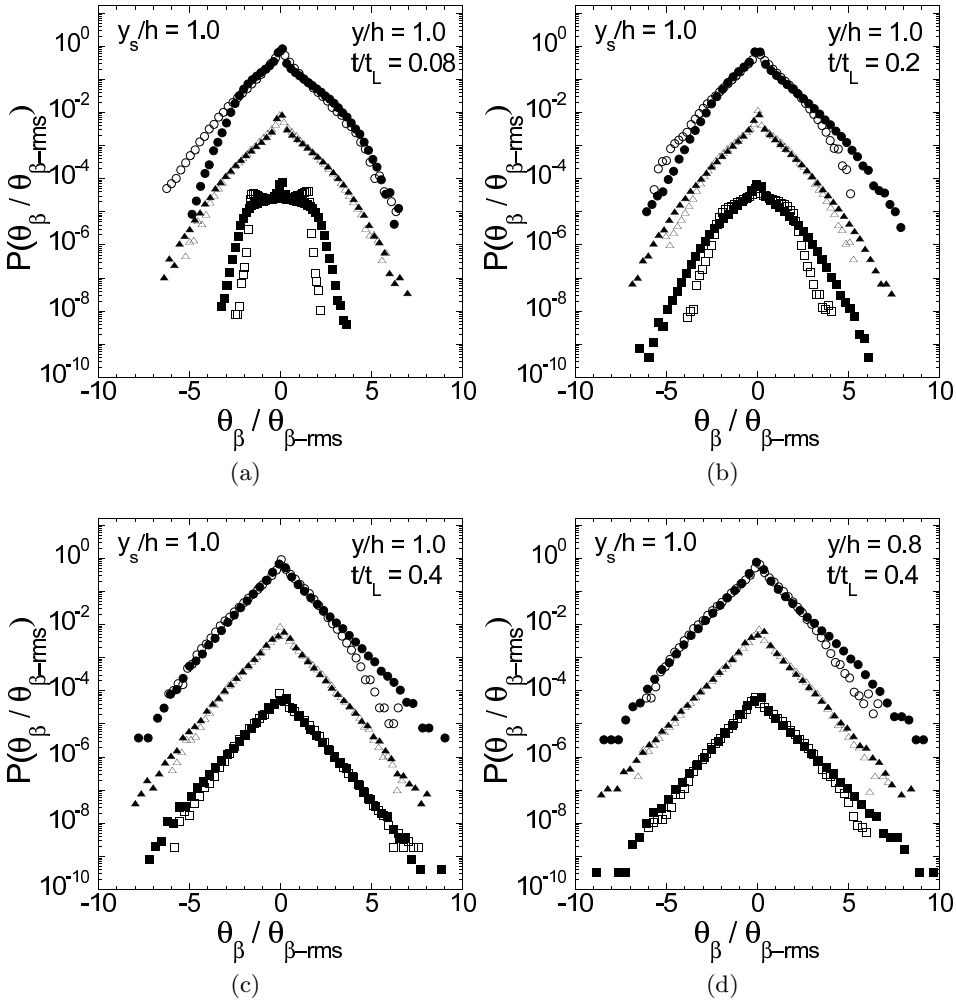

Figure 16: PDFs of the temperature derivatives ($\partial\theta/\partial\beta$ where $\beta = x, y$ or z) for $y_s/h = 1.0$ at three downstream locations: $t/t_L = 0.08$ (a), $t/t_L = 0.2$ (b) and $t/t_L = 0.4$ (c, d) and at two wall-normal locations: $y/h = 1.0$ (a-c) and $y/h = 0.8$ (d). Experimental and DNS results are respectively denoted by the solid symbols ($\partial\theta/\partial x$ (•), $\partial\theta/\partial y$ (■) and $\partial\theta/\partial z$ (▲)) and by the open symbols ($\partial\theta/\partial x$ (○), $\partial\theta/\partial y$ (□) and $\partial\theta/\partial z$ (△)). The curve for $\mathrm{P}[(\partial\theta/\partial x)/(\partial\theta/\partial x)_{rms}]$ is plotted normally, whereas remaining curves are offset downwards in increments of two decades.

In addition, it is worth noting that the quasi-exponential tails appear sooner for the near-wall line source than when the line source is at the centreline.

To further study the evolution of the small-scale scalar field, figure 18 examines the PDFs of ε_θ for the centreline source in figure 18a), and those of the near-wall source in figure 18b). We remark that we plot the PDF of the natural logarithm of ε_θ, $ln(\varepsilon_\theta)$, to verify whether the PDFs of ε_θ exhibit a log-normal distribution, as has been hypothesized (e.g. Gurvich & Yaglom (1967)) and observed in situations where the scalar is injected at large scales (e.g. Sreenivasan *et al.* (1977); Dahm & Buch (1989); Su & Clemens (2003); Schumacher & Sreenivasan (2005); Sutton & Driscoll (2013)), albeit with small

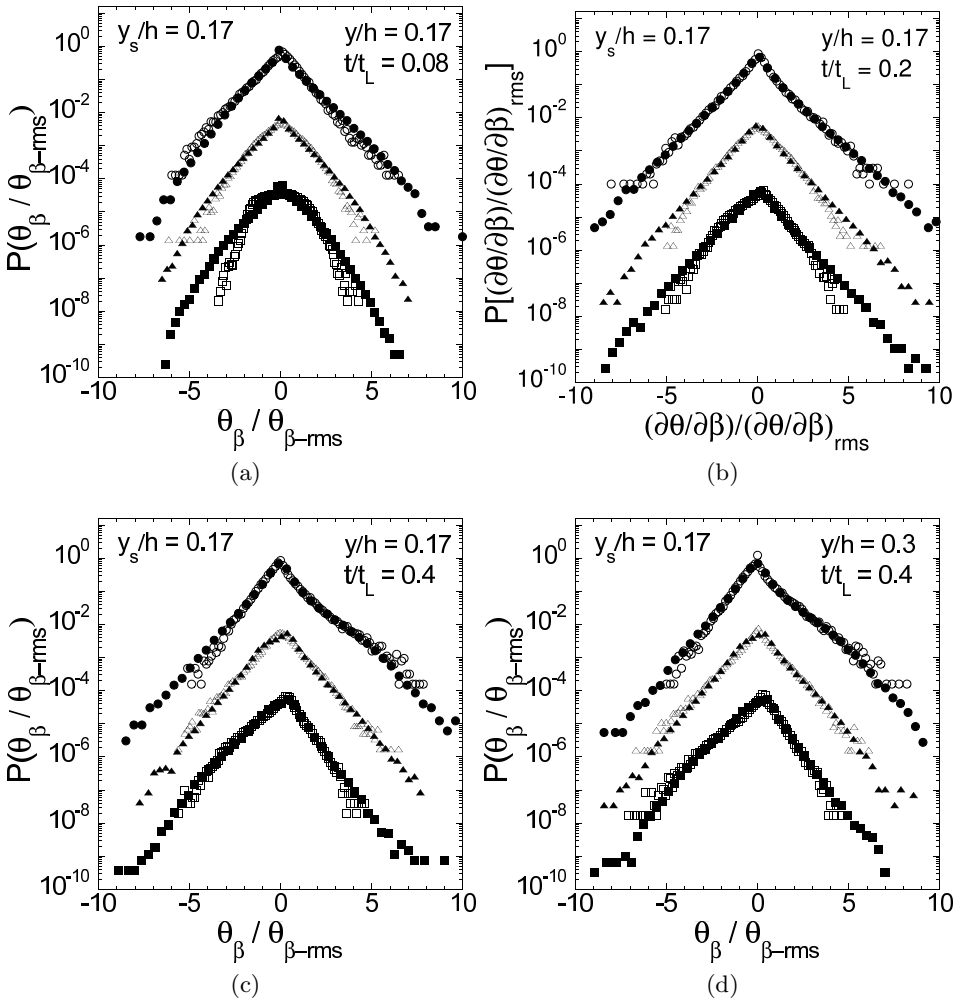

Figure 17: PDFs of the temperature derivatives ($\theta_\beta \equiv \partial\theta/\partial\beta$, where $\beta = x, y$ or z) for $y_s/h = 0.17$ at three downstream locations: $t/t_L = 0.08$ (a), $t/t_L = 0.2$ (b) and $t/t_L = 0.4$ (c, d) for two wall-normal locations: $y/h = 0.17$ (a-c) and $y/h = 0.3$ (d). Experimental and DNSs results are respectively denoted by the solid symbols ($\partial\theta/\partial x$ (•), $\partial\theta/\partial y$ (■) and $\partial\theta/\partial z$ (▲)) and by the open symbols ($\partial\theta/\partial x$ (○), $\partial\theta/\partial y$ (□) and $\partial\theta/\partial z$ (△)). The curve for $\mathrm{P}[(\partial\theta/\partial x)/(\partial\theta/\partial x)_{rms}]$ is plotted normally, whereas remaining curves are offset downwards in increments of two decades.

departures, which may or may not be significant (Holzer & Siggia 1994). Plotting the PDFs in log-linear coordinates i) renders log-normal distributions to appear as concave-down parabolas, and ii) emphasizes the tails of the PDFs. In the most extreme case (closest to the source for $y_s/h = 1.0$), the PDF of ε_θ is clearly not log-normal, having a distinct peak and tails for small values of ε_θ (i.e. their left tails), which verge on exponential behaviour. As previously observed (e.g. Lavertu & Mydlarski (2005)), the centreline plume flaps more because i) it is not bounded on one side (by the wall), and ii) the intensity of the turbulence (and therefore the mixing) is lower at the centreline than it is near the wall, where u_{rms} increases due to increased production of turbulent

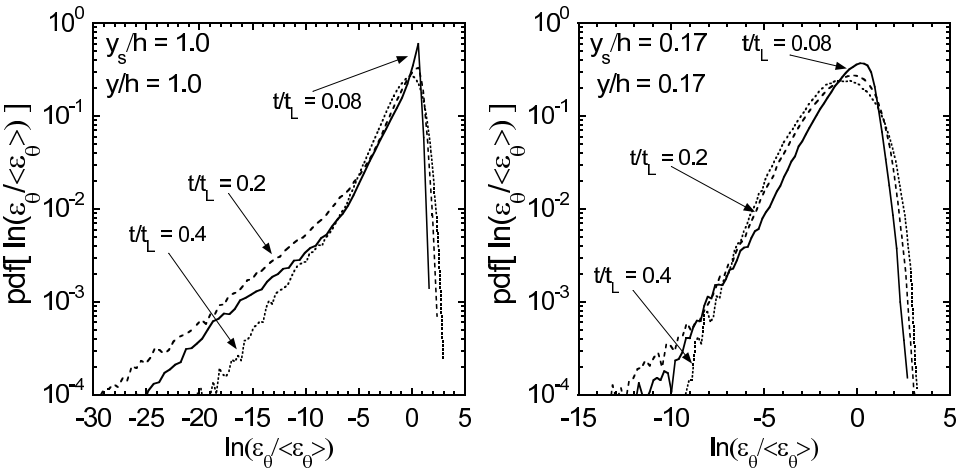

Figure 18: PDFs of (the natural logarithm of) $\varepsilon_\theta/\langle\varepsilon_\theta\rangle$ at $y_s/h = 1.0$ (a), and $y_s/h = 0.17$ (b) for three downstream locations: $t/t_L = 0.08$ (solid line), $t/t_L = 0.2$ (dashed line), and $t/t_L = 0.4$ (dotted line). Only DNS results are presented given that the three components of ε_θ are not measured simultaneously.

kinetic energy. Consequently, the possibility of measuring small values of ϵ_θ for the plume generated by the centreline source is increased due to i) smaller measured temperature differences due to the increased bulk motion of the plume, and ii) increased measurements made outside of the plume. As t/t_L (or equivalently x/h) increases, and as the wall is approached, the PDFs of ε_θ evolve, becoming more log-normal in nature, presumably due to the reduced flapping of the plume (as it widens with increasing t/t_L) and the more intense turbulent mixing that occurs near the wall. Such variations in the shape of the PDF of ε_θ need to be accounted for to accurately model to scalar mixing process, such as that which would occur in a combustion chamber where the fuel is injected at small scales. Assumption of a constant shape (e.g. log-normal) of the PDF of ε_θ would clearly be inaccurate over significant regions of the flow in situations where a scalar is injected at small scales.

7.3. *The evolution of* ε_θ

The instantaneous fields of the (total and three components of the) scalar dissipation rate (i.e., ε_θ, ε_{θ_x}, ε_{θ_y} and ε_{θ_z}), are plotted in figure 19. These are presented to provide qualitative insight into the scalar dissipation rate. In the analysis that follows, we quantitatively discuss the evolution of ε_θ and its components by analyzing specific statistics related to these quantities. For example, it is already evident from figure 19 that the largest contribution to ε_θ comes from ε_{θ_y}. However, one can also observe that its relative contribution to ε_θ decreases with increasing downstream distance, as will be elaborated upon below. We encourage the reader to refer back to these plots for further insight in the course of the subsequent discussion.

Wall-normal profiles of the three components of the scalar dissipation rate are reported in figure 20 for two downstream locations and two source locations, where the scalar dissipation rate has been scaled by $t_L/\langle\Delta T\rangle^2_{ref}$.

For $y_s/h = 1.0$, figure 20 shows that the three components of the scalar dissipation

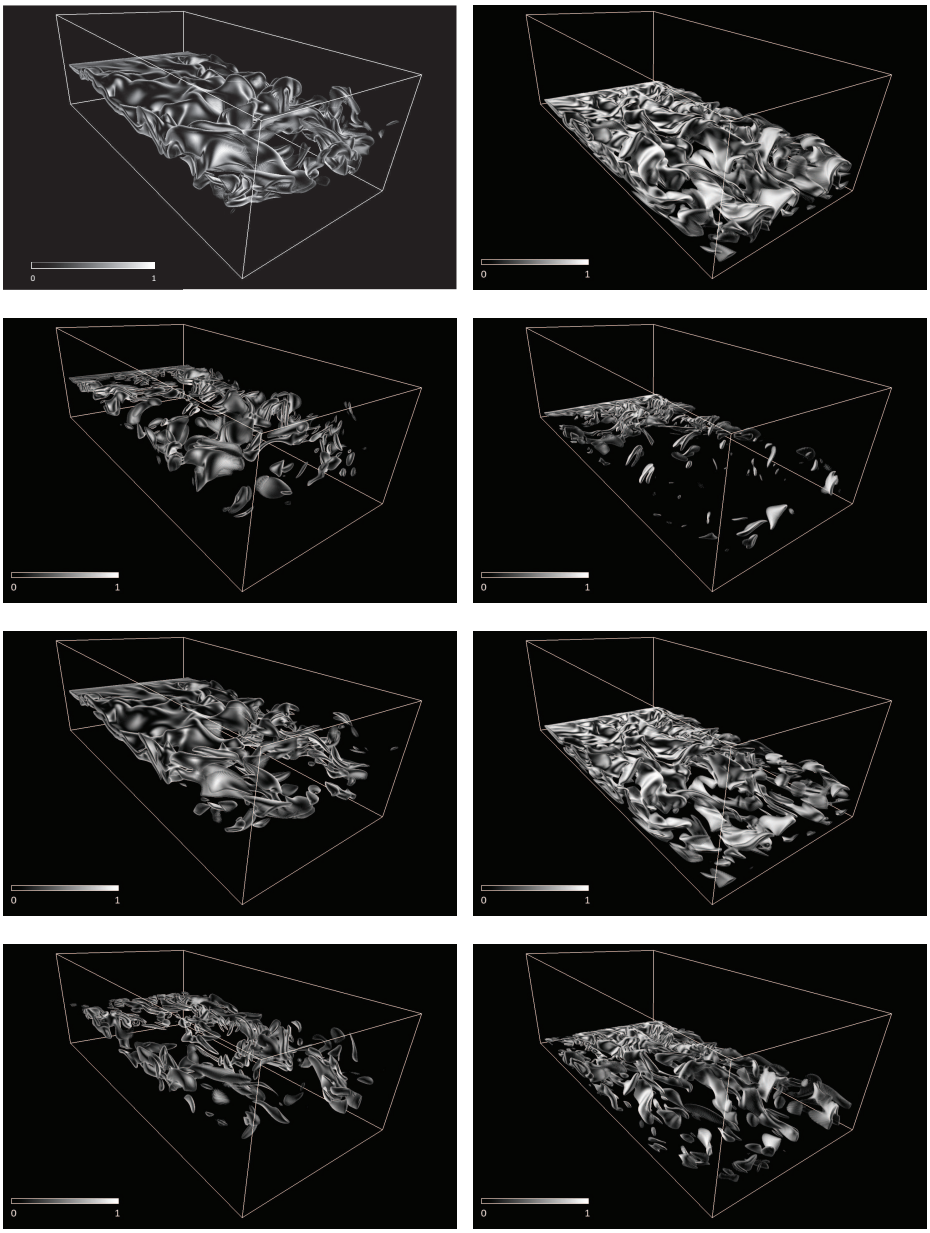

Figure 19: Instantaneous scalar dissipation rate fields – total and individual components – generated (by DNS) downstream of a line source at two wall-normal locations: $y_s/h = 1.0$ (a), (c), (e) and (g); $y_s/h = 0.17$ (b), (d), (f) and (h). $\alpha(\partial\theta/\partial x_i)^2$: (a) and (b). $\alpha(\partial\theta/\partial x)^2$: (c) and (d). $\alpha(\partial\theta/\partial y)^2$: (e) and (f). $\alpha(\partial\theta/\partial z)^2$: (g) and (h). $Re_\tau = 190$. $t^+ = 2770$ for the velocity field and $t^+ = 166$ for the scalar field (where, in the latter case, $t^+ = 0$ corresponds to the time at which the scalar is first injected into the flow). Note that the legends corresponds to the instantaneous scalar dissipation rates non-dimensionalized by $\varepsilon_\theta(t/t_L = 0.08, y/h = 1.0; y_s/h = 1.0)$. Imagery produced by VAPOR (www.vapor.ucar.edu – see also Clyne & Rast (2005); Clyne *et al.* (2007)).

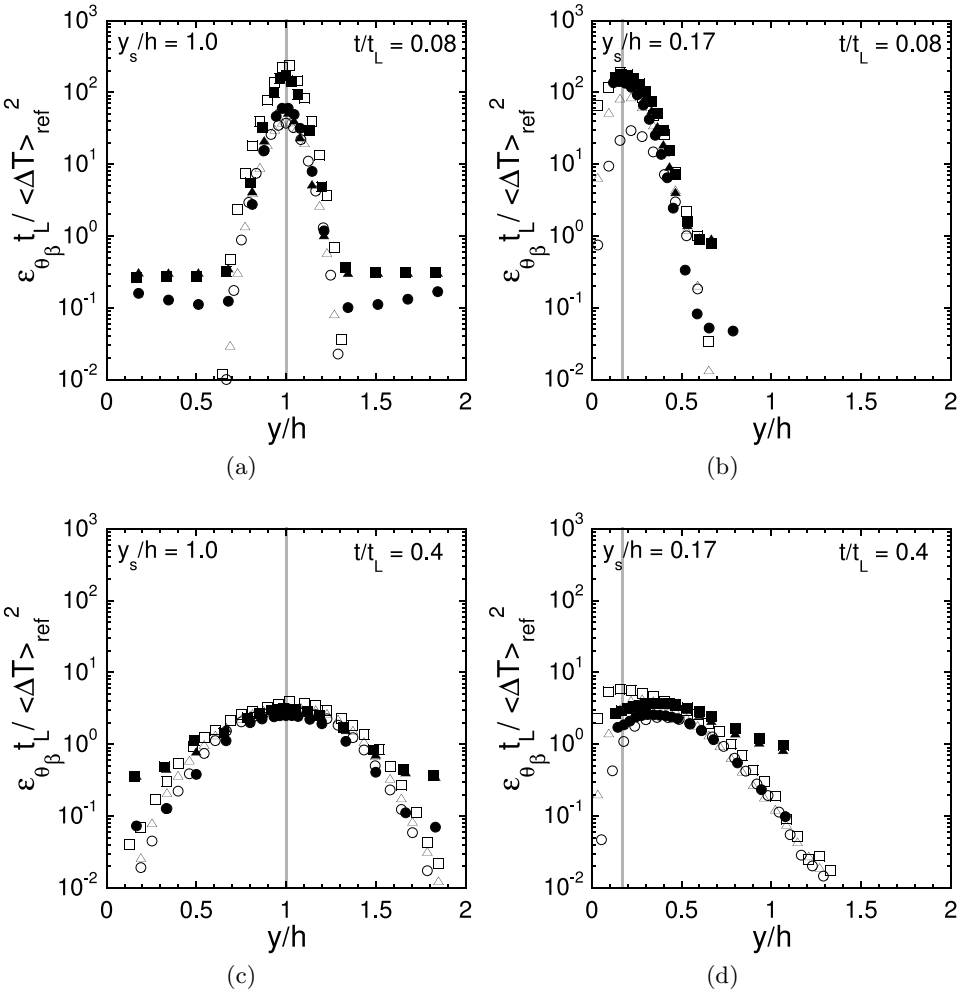

Figure 20: Wall-normal evolutions of the three components of the scalar dissipation rate for $y_s/h = 1.0$ and $y_s/h = 0.17$ at two downstream locations: $t/t_L = 0.08$ (a, b) and $t/t_L = 0.4$ (c, d). Experimental results are denoted by the solid symbols: ε_{θ_x} (•), ε_{θ_y} (■) and ε_{θ_z} (▲) and the numerical results are denoted by the open symbols: ε_{θ_x} (○), ε_{θ_y} (□) and ε_{θ_z} (△). The vertical line indicates the transverse location of the source.

rate have approximately Gaussian profiles with maxima at the channel centreline. Outside the plume, a plateau is observed in the experimental data due to the non-zero ambient noise (i.e. noise measured by the cold-wire thermometer outside of the thermal plume, which includes i) electronic noise, ii) actual temperature fluctuations in the free-stream flow, which is never perfectly isothermal, and iii) a negligible contamination by the velocity fluctuations being erroneously recorded as temperature fluctuations). Small-scale anisotropy is observed near the source ($t/t_L = 0.08$) where $\varepsilon_{\theta_y} > \varepsilon_{\theta_z} \approx \varepsilon_{\theta_x}$. Farther downstream ($t/t_L = 0.4$), the gap between the three components of ε_θ is considerably reduced.

For $y_s/h = 0.17$, figure 20 shows, firstly, that the experimental data appear to be more isotropic, presumably due to their larger Reynolds number, whereas the DNSs data

exhibit differences between the three components ($\varepsilon_{\theta_y} > \varepsilon_{\theta_z} > \varepsilon_{\theta_x}$). Furthermore, the peak of ε_{θ_y} (the largest component) measured from the DNSs remains downstream of the source location for all measurement locations presented herein, whereas the peak of ε_{θ_y} measured in the experiments drifts towards the channel centreline. This may be explained by the prominence in the DNSs of the mechanism of production of ε_{θ_y} due to mean velocity gradients (which, as previously mentioned, will be discussed shortly). The movement in the peak of the scalar dissipation profile recalls the drift observed in the r.m.s. profiles. Note that in both the experiments and the DNSs, the peaks of the ε_{θ_x} and ε_{θ_z} profiles drift towards the centreline as t/t_L is increased (but the rate at which they do so is faster for the experiments). ε_{θ_y} also remains the largest component. Note that if the scalar were injected uniformly, one might expect that the scalar dissipation would peak near the region of maximum shear. (Recall that in a turbulent channel flow, the turbulence intensity is maximum in the buffer layer, i.e. $y^+ \in [5, 30]$. In the present flows, $y^+ = 15$ corresponds to $y/h = 0.03$ and $y/h = 0.08$ in the experiments and the DNSs, respectively.)

The evolution of the peak of the dissipation profile is somewhat similar to the evolution of the peak of the r.m.s. profile (see figure 4(b)). Previous researchers have attempted to establish a parallel between the location of the maximum of dissipation and that of the maximum temperature fluctuations. For instance, Lockwood & Moneib (1980) measured the fluctuating temperature in a heated round turbulent free jet. They showed that the scalar dissipation rate of a turbulent jet attains its maximum at the location of the maximum of the temperature fluctuation intensity. However, this conclusion was contradicted by the observations of Antonia & Mi (1993), who studied the temperature "jumps" (a relatively sudden increase in temperature followed by a gradual decrease – also known as "ramp-cliff" structures) in a heated turbulent jet, and who attempted to estimate their contributions to the temperature dissipation. They showed that although the temperature "jumps" contributed to an increase in the temperature variance, their contribution to the scalar dissipation rate was small.

The downstream evolution of the centreline ($y/h = 1.0$) and the off-centreline ($y/h = 0.8$) mean thermal dissipation is shown in figure 21 for $y_s/h = 1.0$. At the centreline, the experiments and DNS both exhibit a power law-decay of the form $\varepsilon_\theta \sim (t/t_L)^n$, where n varied between -2.2 and -2.0, with the experiments tending to exhibit slightly more negtative decay exponents. Away from the centreline, a power-law decay is also observed, but only after a certain distance downstream ($t/t_L \gtrsim 0.2$), which approximately corresponds to the point at which the plume is wide enough so that the sensor (located at $y/h = 0.8$) no longer measures outside of the plume as it flaps. Analogous plots for the near-wall source are also given in figure 22. As for $y_s/h = 1.0$, the dissipation is maximum in the vicinity of the source and exhibits a power law-decay with similar values of decay exponents, with the experiments again tending to exhibit a slightly more rapid decay. Given the larger values of ε_θ measured in the central region of the plume, one can furthermore conclude that the efficiency in smearing the fluctuations in the scalar field is larger behind the source than at the edges of the plume. However, at the farthest downstream location, the difference between the two is smaller than 8%, indicating that ε_θ tends to become more uniform inside the plume as it expands, as observed in figure 20. We also note that Rosset *et al.* (2001) found $\varepsilon_\theta \sim x^{-2.5}$ downstream of a heated line source placed in a turbulent boundary layer. Their decay exponent, albeit slightly more negative, is quite similar to the values measured herein, despite the differences in flow geometry, Reynolds number, line source location, etc.

To investigate the evolution of the components of the scalar dissipation rate and their anisotropy, figures 23 and 24 plot the evolution of $\varepsilon_{\theta_\beta}/\varepsilon_{\theta_\gamma}$, where the indices β and γ can

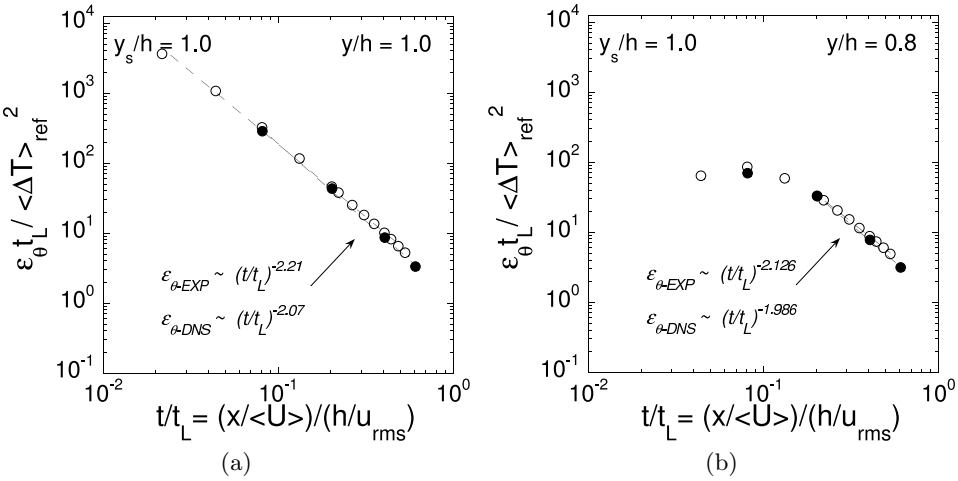

(a) (b)

Figure 21: Downstream evolution of the total scalar dissipation rate for $y_s/h = 1.0$ at two wall-normal locations: $y/h = 1.0$ (a) and $y/h = 0.8$ (b). Experimental results are denoted by the solid symbols and the numerical results are denoted by the open symbols. The solid line and dashed line are the best-fit power laws to the experimental and numerical data, respectively.

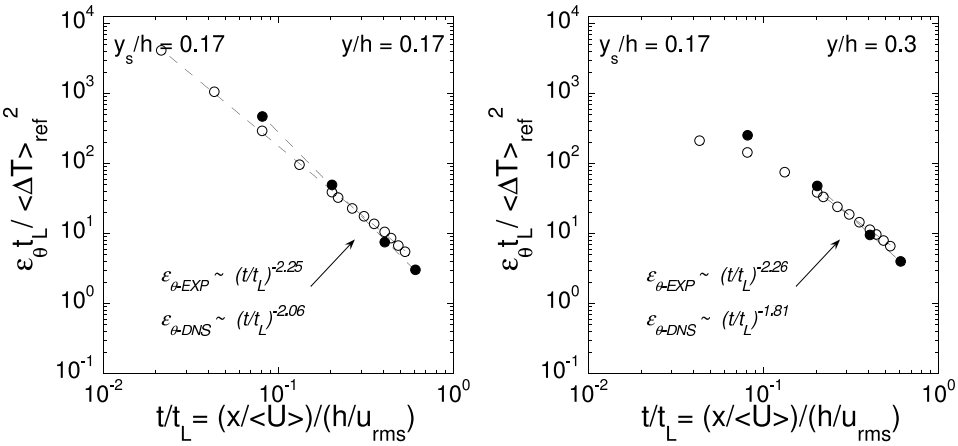

(a) (b)

Figure 22: Downstream evolution of the total scalar dissipation rate for $y_s/h = 0.17$ at two wall-normal locations: $y/h = 0.17$ (a) and $y/h = 0.3$ (b). Experimental results are denoted by the solid symbols and the numerical results are denoted by the open symbols. The solid line and dashed line are the best-fit power laws to the experimental and numerical data, respectively.

be x, y or z, and where $\beta \neq \gamma$. For a locally isotropic scalar field, this ratio must be equal 1. When the line source is at the centreline, both the experiments and the DNSs show that the anisotropy is reduced and the components of the scalar dissipation rates converge towards an isotropic state. Near the source, however, the dissipation is predominantly in the y-direction due to the sharp temperature gradients ($\partial\theta/\partial y$) there that are associated

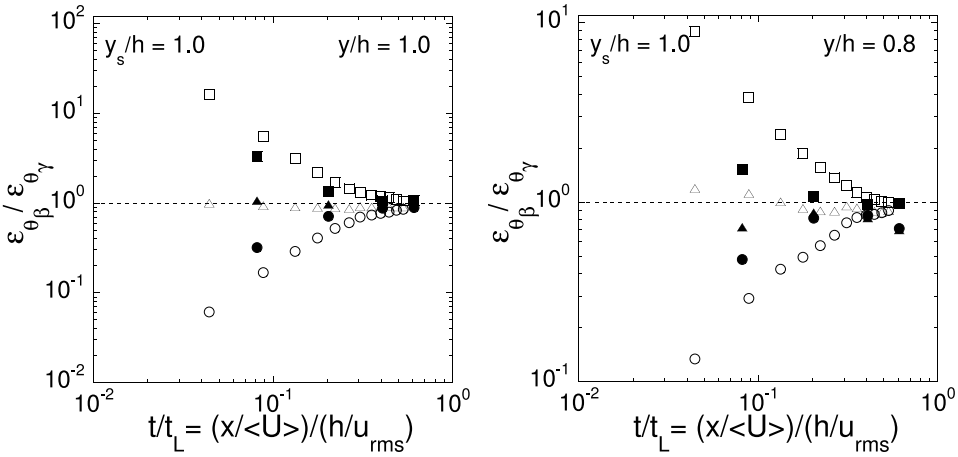

(a) (b)

Figure 23: Downstream evolution of the ratios $\varepsilon_{\theta_\beta}/\varepsilon_{\theta_\gamma}$ (where β and $\gamma = x, y$ or z and $\beta \neq \gamma$) for $y_s/h = 1.0$ at two wall-normal locations: $y/h = 1.0$ (a) and $y/h = 0.8$ (b). Experimental results are denoted by the solid symbols: $\varepsilon_{\theta_x}/\varepsilon_{\theta_y}$ (●), $\varepsilon_{\theta_y}/\varepsilon_{\theta_z}$ (■) and $\varepsilon_{\theta_x}/\varepsilon_{\theta_z}$ (▲) and the numerical results are denoted by the open symbols: $\varepsilon_{\theta_x}/\varepsilon_{\theta_y}$ (○), $\varepsilon_{\theta_y}/\varepsilon_{\theta_z}$ (□) and $\varepsilon_{\theta_x}/\varepsilon_{\theta_z}$ (△).

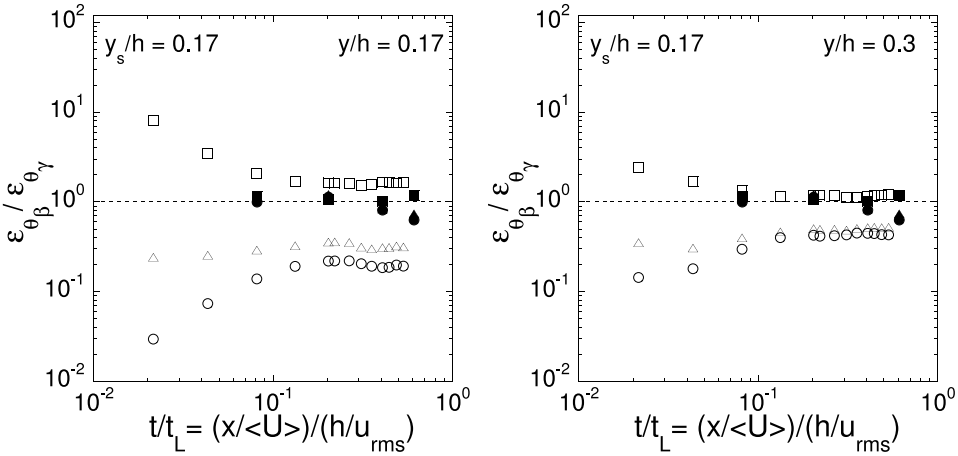

(a) (b)

Figure 24: Downstream evolution of the ratios $\varepsilon_{\theta_\beta}/\varepsilon_{\theta_\gamma}$ (where β and $\gamma = x, y$ or z and $\beta \neq \gamma$) for $y_s/h = 0.17$ at two wall-normal locations: $y/h = 0.17$ (a) and $y/h = 0.3$ (b). Experimental results are denoted by the solid symbols: $\varepsilon_{\theta_x}/\varepsilon_{\theta_y}$ (●), $\varepsilon_{\theta_y}/\varepsilon_{\theta_z}$ (■) and $\varepsilon_{\theta_x}/\varepsilon_{\theta_z}$ (▲) and the numerical results are denoted by the open symbols: $\varepsilon_{\theta_x}/\varepsilon_{\theta_y}$ (○), $\varepsilon_{\theta_y}/\varepsilon_{\theta_z}$ (□) and $\varepsilon_{\theta_x}/\varepsilon_{\theta_z}$ (△).

with the plume boundary. The dissipation in the two other directions ($\partial\theta/\partial x$ and $\partial\theta/\partial z$) are almost equal, indicative of the quasi-axisymmetric nature of the turbulence at that location. For the near-wall source, figure 24 indicates that i) the agreement between the experiments and the DNSs is not as good as it is for the centreline source, with the

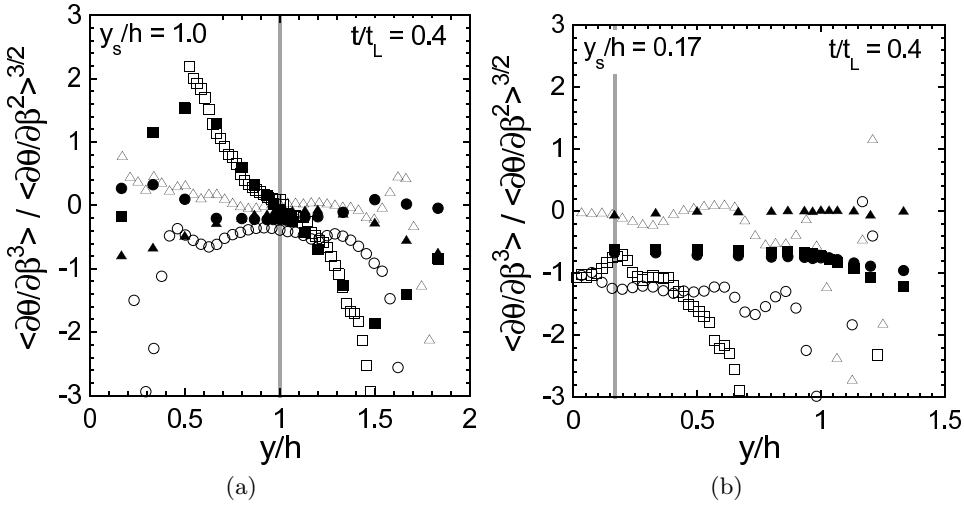

Figure 25: Transverse profiles of the skewness of the scalar derivative, $S_{\partial\theta/\partial\beta} \equiv \langle(\partial\theta/\partial\beta)^3\rangle/\langle(\partial\theta/\partial\beta)^2\rangle^{3/2}$, where β is equal to x, y or z, at $t/t_L = 0.4$. (a) $y_s/h = 1.0$. (b) $y_s/h = 0.17$. Experiments (solid symbols) and DNSs (open symbols) are reported. $S_{\partial\theta/\partial x}$, (● and ○); $S_{\partial\theta/\partial y}$, (■ and □); $S_{\partial\theta/\partial z}$, (▲ and △), respectively. The vertical line indicates the transverse location of the source.

experiments being notably more isotropic than the DNSs. Furthermore, note that the anisotropy is stronger when measured at $y/h = 0.17$ than at $y/h = 0.3$, indicating that there exists regions in the channel flow field that better lend themselves to returning to an isotropic state. We will subsequently argue that the anisotropy is dependent on the presence of velocity gradients (Antonia & Browne 1986; Gonzalez 2000), as well as the Reynolds number of the flow. In this vein, we remark that the anisotropy measured in the experiments is less strong than in the DNSs, presumably due to its larger Reynolds numbers, which i) results from a more rapid elimination of the large-scale anisotropy associated with the injection of the scalar, and ii) explains the discrepancies observed in figure 24. Moreover, note that the flow is no longer (quasi-) homogeneous in the regions plotted in figure 24, so the equal offset of the anisotropy of ε_{θ_y} by ε_{θ_x} and ε_{θ_z} is not observed here (like in figure 23). Regarding these figures, we finally note that the measured increase in anisotropy observed in figures 23(b) and 24 is presumably due to experimental errors arising from the low signal-noise ratio at the farthest downstream location ($t/t_L = 0.6$).

The small-scale anisotropy of the scalar field can also be examined using third-order statistics – most notably the skewness of the scalar derivative, which must be zero in a locally isotropic flow. Figure 25 plots the transverse profiles of the skewness of $(\partial\theta/\partial\beta)$, $S_{\partial\theta/\partial\beta} \equiv \langle(\partial\theta/\partial\beta)^3\rangle/\langle(\partial\theta/\partial\beta)^2\rangle^{3/2}$, where β is equal to x, y or z. When $y_s/h = 1.0$, we observe that $S_{\partial\theta/\partial x}$ and $S_{\partial\theta/\partial z}$ are close to zero in the inner core of the plume, where the former is consistent with local isotopy, but the latter simply being symptomatic of the homogeneity of the flow in the z-direction. $S_{\partial\theta/\partial y}$ is an odd function of y/h due to the underlying symmetries of the flow when $y_s/h = 1.0$, and changes sign depending on which side of the flapping plume the sensor is located. Thus, its zero value at $y/h = 1.0$ does not result from local isotropy at that location, but is rather a consequence of the underlying symmetries in this case. When $y_s/h = 0.17$, persistent anisotropy in $S_{\partial\theta/\partial x}$

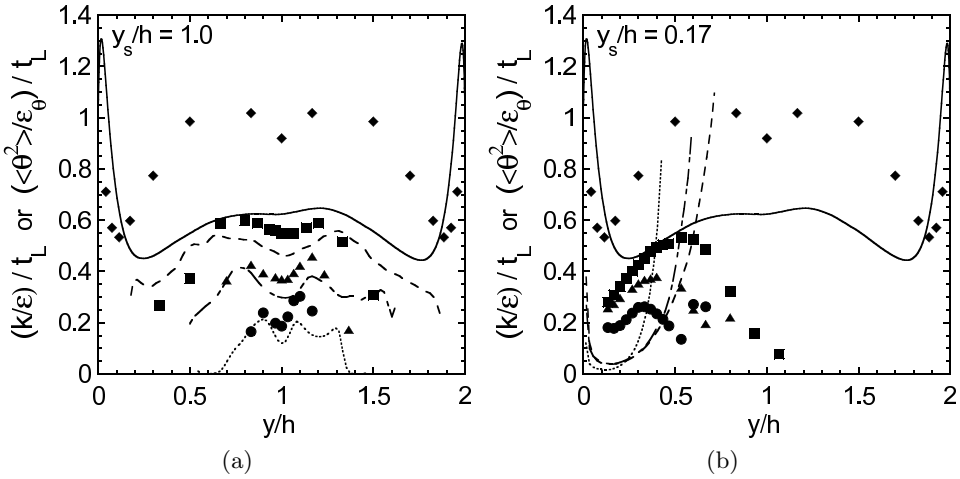

Figure 26: Transverse profiles of the mechanical and thermal time scales normalized by t_L. (a) $y_s/h = 1.0$. (b) $y_s/h = 0.17$. Lines are DNS results, symbols are experimental ones. $(k/\varepsilon)/t_L$: solid line or ♦. $(\langle\theta^2\rangle/\varepsilon_\theta)/t_L$ at $t/t_L = 0.08$: dotted line or •. $(\langle\theta^2\rangle/\varepsilon_\theta)/t_L$ at $t/t_L = 0.2$: dot-dashed line or ▲. $(\langle\theta^2\rangle/\varepsilon_\theta)/t_L$ at $t/t_L = 0.4$: dashed line or ■.

and $S_{\partial\theta/\partial y}$ is observed, although it is i) lesser in magnitude for the experimental data, and ii) more uniform over the extent of the plume. However, $S_{\partial\theta/\partial z}$ is zero in both cases once again, as expected.

From figures 23 and 24, one observes that the end of the period of isotropization occurs within a few tenths of $t_L(\equiv h/u_{rms})$. It is therefore of interest to see how this time scale relates to the mechanical or thermal time scales of the flow. To this end, figure 26 plots the transverse profiles of both the (experimental and numerical) mechanical and thermal time scales normalized by t_L: $(k/\varepsilon)/t_L$ and $(\langle\theta^2\rangle/\varepsilon_\theta)/t_L$, respectively. The latter are plotted at three downstream locations (t/t_L =0.08, 0.2 and 0.4), whereas the former is the same for all downstream distances in this fully-developed flow. We firstly remark that t_L is directly related to the mechanical time scale, $k/\varepsilon \equiv \frac{1}{2}\langle u_i u_i\rangle/2v\langle s_{ij}s_{ij}\rangle \approx \frac{3}{2}u_{rms}^2/(u_{rms}^3/\ell) \sim \ell/u_{rms} \sim h/u_{rms} = t_L$. Thus it is reasonable for k/ε and t_L to be of the same order, which we observe (quite closely for the experiments, and within a factor of ~ 1.5 for the simulations). This difference is due to the fact that, in the above approximation, $C_\varepsilon(\equiv \varepsilon/(u_{rms}^3/\ell))$ is not a constant but a decreasing function of Reynolds number (in the range of moderate Reynolds numbers characterizing the present work, Sreenivasan (1984); Donzis *et al.* (2005)) such that $k/\varepsilon \sim C_\varepsilon t_L$ before C_ε has reached its asymptotic value.

Given this, one can conclude that isotropization of the scalar field occurs, more or less, within a few tenths of the *mechanical time scale*, implying that it may not be the most relevant scale. With respect to the thermal time scale, we remark that because $t_L \approx k/\varepsilon$, $(\langle\theta^2\rangle/\varepsilon_\theta)/t_L$ can be interpreted as a thermal-to-mechanical time-scale ratio. In the present work, we observe that the thermal time scale is initially notably smaller than the mechanical one – of the same order as the return-to-isotropy time scale, *viz.* tenths of t_L. It then increases with downstream distance, tending towards $(k/\varepsilon)/t_L$, *except* near the wall in the simulations. In the other cases, the increase in $(\langle\theta^2\rangle/\varepsilon_\theta)/t_L$ is consistent with a plume injected at small scales, which proceeds to grow, and ultimately, occupy then entire cross-section of the channel, taking on a time scale similar to that of the hydrodynamic

field. However, near the wall for the simulations, which are at a lower Reynolds number than the experiments, we observe $(\langle\theta^2\rangle/\varepsilon_\theta)/t_L$ to be roughly independent of t/t_L. This observation is consistent with the notion that close to the wall, at low Reynolds numbers, another phenomenon is dictating the mixing process. As we shall argue momentarily, it is most likely that this phenomenon is the production of ε_{θ_y} due to the mean velocity gradient, which is presumably controlling the thermal time scale and may explain why $(\langle\theta^2\rangle/\varepsilon_\theta)/t_L$ is not evolving with downstream distance (t/t_L) in that region. However, when isotropization occurs, $(\langle\theta^2\rangle/\varepsilon_\theta)/t_L$ appears to increase, possibly asymptoting to $(k/\varepsilon)/t_L$. We also note that Rosset *et al.* (2001) and Gonzalez & Paranthoën (2003) argued that the thermal time scale may be more relevant to the mixing / isotropization process than the mechanical one. Furthermore, Gonzalez & Paranthoën (2003) noted that $(\langle\theta^2\rangle/\varepsilon_\theta) \sim (\ell_\theta/k_\theta^{1/2})$, where k_θ represents the kinetic energy of the flow structures of size ℓ_θ, which, in this case, falls between the Kolmogorov and integral length scales. Thus $\ell_\theta/k_\theta^{1/2}$ can also be interpreted as a time scale related to the (inverse of the) vorticity at the scale ℓ_θ. Lastly, we observe a reasonable agreement between the experimental and numerical results for the thermal time scale in the case of the centreline source. Near the wall, the difference may be due to the larger effect (in this region) of the difference in Reynolds numbers between the two sets of data, as already noted. Furthermore, the factor of ~ 1.5 between the experimental and numerical data for the mechanical time scale may also derive from the different Reynolds numbers of the flow, and thus possible different values for the non-dimensional constants in the above approximation relating k/ε to t_L.

To further study the return to isotropy (or the lack of a return, in the case of the simulations of the plume emitted from a near-wall source), consider the evolution equation of the scalar dissipation rate, given by

$$\begin{aligned}\frac{\partial\varepsilon_\theta}{\partial t} + \langle U_j\rangle\frac{\partial\varepsilon_\theta}{\partial x_j} = &\overbrace{-2\alpha\frac{\partial\langle U_j\rangle}{\partial x_i}\langle\frac{\partial\theta}{\partial x_i}\frac{\partial\theta}{\partial x_j}\rangle}^{\mathcal{P}} - 2\alpha\frac{\partial\langle T\rangle}{\partial x_j}\langle\frac{\partial u_j}{\partial x_i}\frac{\partial\theta}{\partial x_i}\rangle \\ &- 2\alpha\langle u_j\frac{\partial\theta}{\partial x_i}\rangle\frac{\partial^2\langle T\rangle}{\partial x_i\partial x_j} - 2\alpha\langle\frac{\partial u_j}{\partial x_i}\frac{\partial\theta}{\partial x_i}\frac{\partial\theta}{\partial x_j}\rangle \\ &+ \frac{\partial}{\partial x_j}\left(\alpha\frac{\partial\langle\varepsilon_\theta\rangle}{\partial x_j} - \langle u_j\varepsilon_\theta\rangle\right) - \underbrace{2\alpha^2\langle\frac{\partial^2\theta}{\partial x_i\partial x_j}\frac{\partial^2\theta}{\partial x_i\partial x_j}\rangle}_{\Gamma},\end{aligned} \tag{7.1}$$

(where repeated indices imply Einstein's summation convention). In the limit of large Reynolds and Péclet numbers, it is hypothesized (Corrsin 1953; Tennekes & Lumley 1972) that the above equation simplifies to a balance between the production of ε_θ due to stretching of the scalar gradients by the turbulent strain rate $(2\alpha\langle\frac{\partial u_j}{\partial x_i}\frac{\partial\theta}{\partial x_i}\frac{\partial\theta}{\partial x_j}\rangle)$ and the destruction of ε_θ by molecular processes $(\Gamma = 2\alpha^2\langle\frac{\partial^2\theta}{\partial x_i\partial x_j}\frac{\partial^2\theta}{\partial x_i\partial x_j}\rangle)$. However, at finite Reynolds and Péclet numbers, other terms may be relevant. To investigate and explain the previously observed anisotropy, we focus on the two terms $\mathcal{P}(=\mathcal{P}_x+\mathcal{P}_y+\mathcal{P}_z)$ and $\Gamma(=\Gamma_x+\Gamma_y+\Gamma_z)$. The former is the production of ε_θ by mean velocity gradients, and the latter quantifies the dissipation of ε_θ by molecular processes, as just noted. For channel flow, the components of these two terms are: $\mathcal{P} = \mathcal{P}_y = -2\alpha\partial\langle U\rangle/\partial y\langle(\partial\theta/\partial y)(\partial\theta/\partial x)\rangle$ with $\mathcal{P}_x = \mathcal{P}_z = 0$ and $\Gamma_x = 2\alpha^2[\langle(\partial^2\theta/\partial x^2)^2\rangle + \langle(\partial^2\theta/\partial x\partial y)^2\rangle + \langle(\partial^2\theta/\partial x\partial z)^2\rangle]$, $\Gamma_y = 2\alpha^2[\langle(\partial^2\theta/\partial y\partial x)^2\rangle + \langle(\partial^2\theta/\partial y^2)^2\rangle + \langle(\partial^2\theta/\partial y\partial z)^2\rangle]$ and $\Gamma_z = 2\alpha^2[\langle(\partial^2\theta/\partial z\partial x)^2\rangle + \langle(\partial^2\theta/\partial z\partial y)^2\rangle + \langle(\partial^2\theta/\partial z^2)^2\rangle]$. Figure 27 shows the wall-normal profile of the three com-

ponents of Γ and $\mathcal{P}_y$, for the two source locations ($y_s/h = 1.0$ and 0.17) at three downstream positions ($t/t_L = 0.08,\ 0.2$ and 0.4). Note that the y- and z-components of Γ were not accessible experimentally as $\partial\theta/\partial y$ and $\partial\theta/\partial z$ were not simultaneously measured. Furthermore, combined statistical moments of both the velocity and temperature derivatives are not computed due to the fact that the velocity and temperature field are not calculated nor measured simultaneously in the present approach. This thus precludes any comparison of $\mathcal{P}$ with the other leading-order term in equation (7.1).

The mean velocity gradient that exists in the wall-normal direction only, contributes to the production of ε_θ (in the y-direction). The relative importance of this production depends on the wall-normal location within the channel. As the mean velocity gradient ($\partial\langle U\rangle/\partial y$) is small in the centre of the channel, there is very little production of the scalar dissipation by the mean velocity field in the central region (and none at the channel mid-plane, by symmetry). On the other hand, the contribution of $\mathcal{P}_y$ to ε_{θ_y} is not negligible in the near-wall region, as the velocity gradients are large there. In fact, figure 27 shows that the production of dissipation in the wall-normal direction is of the same order of magnitude as Γ_y near the walls. The figure also shows that $\mathcal{P}_y$ does not contribute to the evolution of ε_{θ_y} (or ε_θ) when the source is at the centreline, as expected. Lastly, this production of ε_θ due to mean velocity gradients now explains the aforementioned *i*) persistent anisotropies for the near-wall scalar fields (figure 24), and *ii*) the persistence of a maximum in ε_{θ_y} near the wall (figure 20). In addition, it may possibly explain the constancy of the thermal time scale near the wall, when $y_s/h = 0.17$, as observed in figure 26b).

Johansson & Wikström (1999) performed DNSs of turbulent channel flow with an imposed mean scalar gradient. In the near-wall region, they showed that the two mean gradient production terms (i.e. the first and second terms on the right hand side of equation (7.1)) as well as the term that is the scalar-field analogue to the vortex-stretching term in the turbulent enstrophy budget (i.e. the fourth term in the right hand side of equation (7.1)) contribute the most to the production of ε_θ. These results agree with those presented herein.

Anisotropy invariant maps for ε_θ (Antonia & Kim 1994) are plotted in figures 28-30 where the three solid lines are (often referred to as) the Lumley triangle (Lumley 1978). This triangle is delimited by the following three curves (in the (III, $-II$) plane):

$$III = -\frac{II}{3} - \frac{1}{27}, \tag{7.2}$$

$$III = -2\left(\frac{II}{3}\right)^{3/2}, \tag{7.3}$$

$$III = 2\left(\frac{II}{3}\right)^{3/2}. \tag{7.4}$$

II and III are the second and third invariants of the scalar dissipation rate anisotropy tensor defined as:

$$t_{ij} = \alpha\frac{\langle\frac{\partial\theta}{\partial x_i}\frac{\partial\theta}{\partial x_j}\rangle}{\langle\varepsilon_\theta\rangle} - \frac{1}{3}\delta_{ij}, \tag{7.5}$$

where δ_{ij} is the Kronecker delta. The second and third invariants are given by:

$$II = -\frac{1}{2}t_{ij}t_{ji}, \tag{7.6}$$

$$III = \frac{1}{3}t_{ij}t_{jk}t_{ki}. \tag{7.7}$$

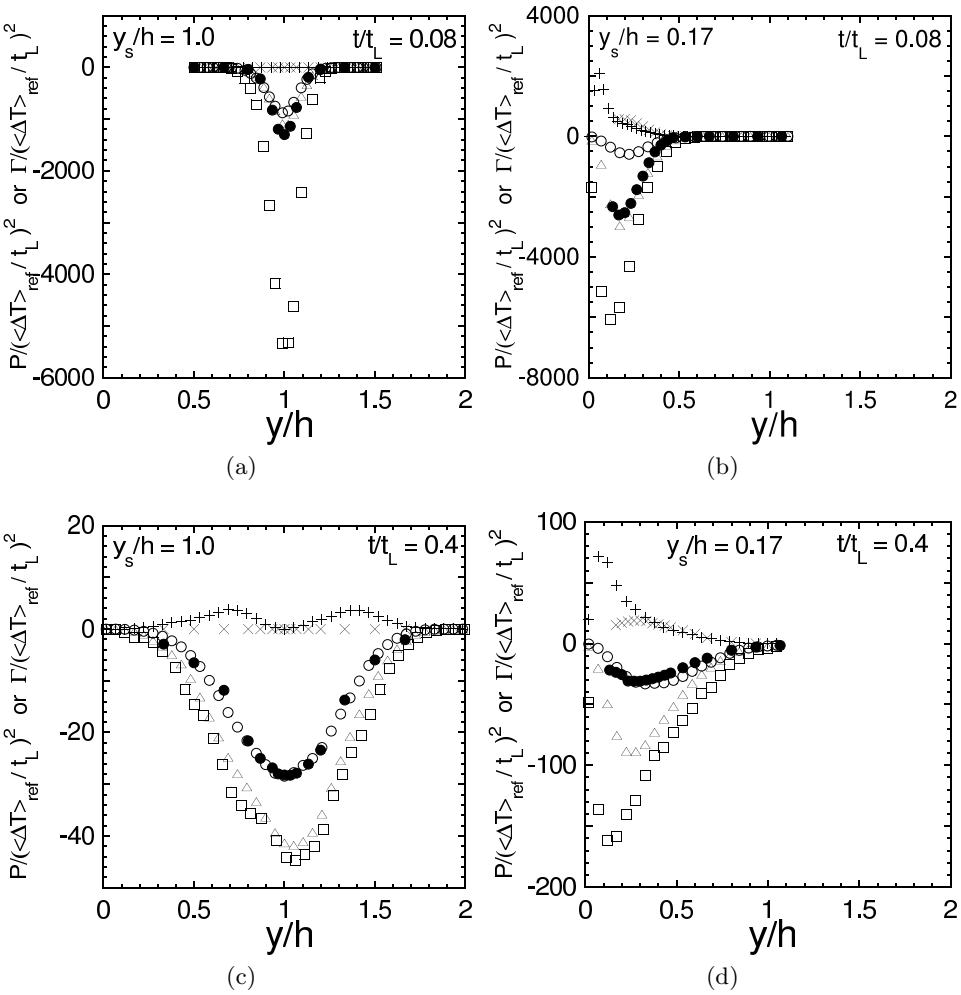

Figure 27: Wall-normal evolution of the y-component of the production of ε_θ by the three components of the dissipation of ε_θ and by the mean velocity gradient for $y_s/h = 1.0$ and $y_s/h = 0.17$ at two downstream locations: $t/t_L = 0.08$ (a, b) and $t/t_L = 0.4$ (c, d). Experimental results are denoted by the solid symbols: $-2\alpha^2\left(\langle(\partial^2\theta/\partial x^2)^2\rangle + \langle(\partial^2\theta/\partial x\partial y)^2\rangle + \langle(\partial^2\theta/\partial x\partial z)^2\rangle\right)$ ($\bullet$) and the numerical results are denoted by the open symbols: $-2\alpha^2\left[\langle(\partial^2\theta/\partial x^2)^2\rangle + \langle(\partial^2\theta/\partial x\partial y)^2\rangle + \langle(\partial^2\theta/\partial x\partial z)^2\rangle\right]$ ($\circ$), $-2\alpha^2\left[\langle(\partial^2\theta/\partial y\partial x)^2\rangle + \langle(\partial^2\theta/\partial y^2)^2\rangle + \langle(\partial^2\theta/\partial y\partial z)^2\rangle\right]$ ($\square$), $-2\alpha^2\left[\langle(\partial^2\theta/\partial z\partial x)^2\rangle + \langle(\partial^2\theta/\partial z\partial y)^2\rangle + \langle(\partial^2\theta/\partial z^2)^2\rangle\right]$ ($\triangle$). The production of dissipation $-2\alpha\langle U\rangle_y\langle(\partial\theta/\partial y)(\partial\theta/\partial x)\rangle$ is also reported for the experiments ($\times$) and the DNSs ($+$).

The plot of $-II$ versus III represents all the possible states that characterize the tensor t_{ij}. Curves (7.3) and (7.4) are respectively the right and left "axisymmetric" boundaries of the anisotropic invariant map. The vertex $II = III = 0$ characterizes the isotropic state. The top right vertex of the line given by equation (7.2) represents the one-component state and the bottom left vertex represents the two-component state.

The return to isotropy behind a centreline source (figure 28(a)) is i) clearly axisymmet-

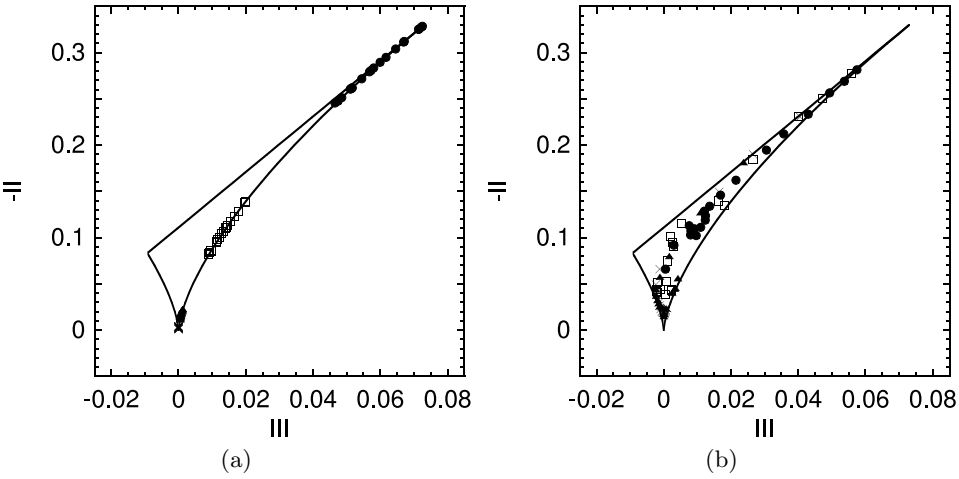

Figure 28: Anisotropy invariant map of ε_θ for $y_s/h = 1.0$ (a) and $y_s/h = 0.17$ (b). Statistics were computed at $t/t_L = 0.02$ ($\circ$), 0.08 ($\square$), 0.2 ($\triangle$) and 0.4 ($\times$) and for $y/h \in [0.8, 1.2]$ (a) and $y/h \in [0.0, 0.4]$ (b).

ric, consistent with the previous results of figure 23, and *ii*) more rapid than that of the scalar field behind the near-wall source. The axisymmetry of the scalar field behind the centreline line source is more clearly observed in figure 29, which shows a very large level of axisymmetry at $y/h = 1.0$, but a slightly smaller degree of axisymmetry at $y/h = 0.8$. These results should be contrasted with those of figure 30, which depict the anisotropy invariant maps for different wall-normal locations for the scalar field generated by the near-wall source. Of particular interest is the evolution from a one-dimensional state very close to the wall (Antonia & Kim 1994) in figure 30(c) to an almost axisymmetric state farther away from the wall in figure 30(d).

7.4. *Conditional statistics*

To gain further insight into the dependence of the scalar dissipation rate, ε_θ, on the scalar fluctuations, θ, which is of particular use in PDF models of scalar mixing, we examine the expectation of $\varepsilon_{\theta_\beta}$ conditioned on individual values of θ, i.e. $\langle \varepsilon_{\theta_\beta} | \theta \rangle$, where $\varepsilon_{\theta_\beta}$ is the β-component of the scalar dissipation ($\beta = x,\ y$ or z). Theoretical work has shown that the form of the conditional expectation profiles, $\langle \varepsilon_\theta | \theta \rangle$, depends on the PDF of the scalar fluctuation, θ (Pope & Ching 1993). A Gaussian PDF of θ is associated with ε_θ and θ being independent. In this case, $\langle \varepsilon_\theta | \theta \rangle$ is found to be a constant (e.g. Anselmet *et al.* 1994, figure 9*b*). A super-Gaussian PDF of the scalar is associated with a rounded, concave-up V-shape for the profile (Sinai & Yakhot 1989; Jayesh & Warhaft 1992) whereas a sub-Gaussian PDF is associated with a rounded concave-down V-shape for the profile (Mydlarski 2003).

Figures 31a) and c) plot the expected value of the various components of the scalar dissipation rate conditioned on the temperature fluctuations for $y_s/h = 1.0$. In the present work, the scalar dissipation rate conditioned on the scalar fluctuation exhibit a concave-down, rounded V-shape. Such a shape indicates that large values of the scalar fluctuation are associated with low values of the scalar dissipation. Each plot begins with an approximately linear departure from $\theta/\theta_{rms} \approx -1.5$, increasing to a maximum, after which the conditional expectation begins to decrease. The double peaks of $\langle \varepsilon_{\theta_y} | \theta \rangle$ measured in

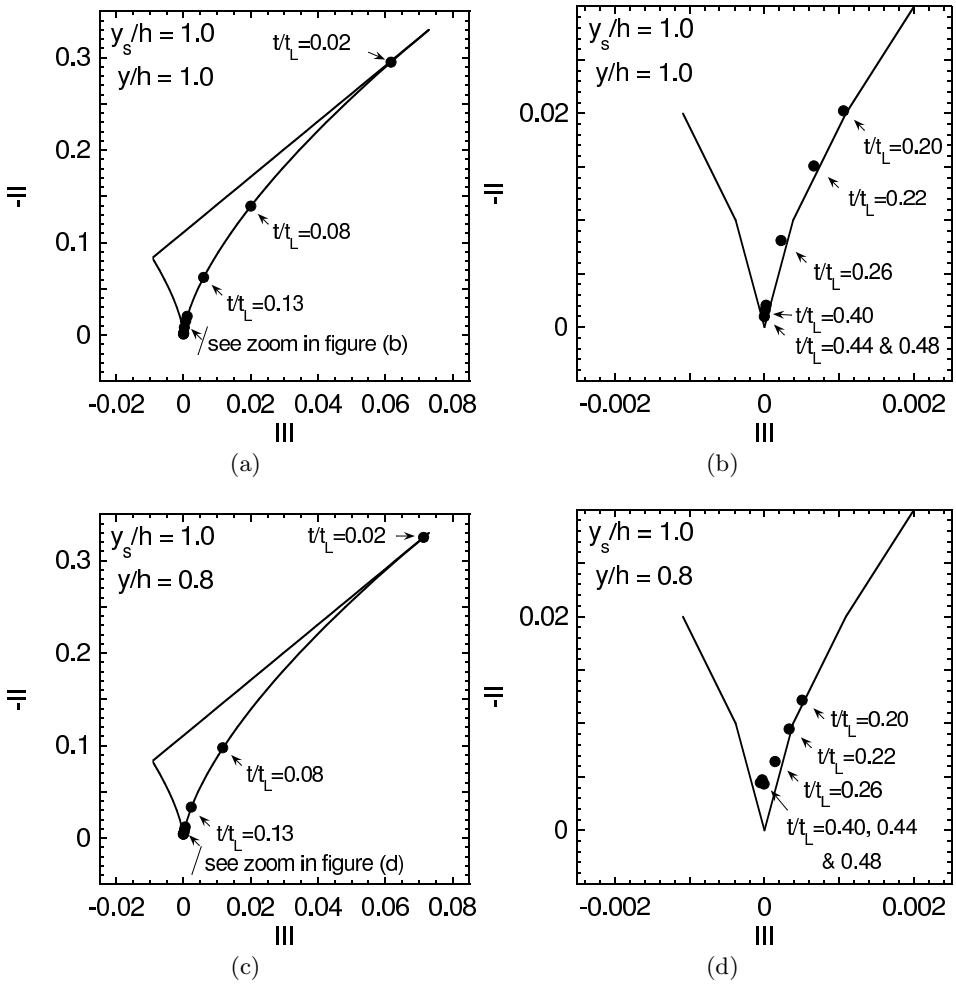

Figure 29: Anisotropy invariant map of ε_θ for $y_s/h = 1.0$ and $y/h = 1.0$ (a). A close-up of figure (a) is presented in figure (b). Anisotropy invariant map of ε_θ for $y_s/h = 1.0$ and $y/h = 0.8$ (c). A close-up of figure (c) is presented in figure (d). Statistics were computed from $t/t_L = 0.02$ to 0.48.

the experiments in the vicinity of the source disappear farther downstream. These may be related to the previously discussed PDFs of $\partial\theta/\partial y$, which were shown to be bi- or trimodal near the source (see figure 16).

Figures 31b) and d) plot the conditional expectation $\langle\varepsilon_{\theta_\beta}|\theta/\theta_{rms}\rangle/\langle\varepsilon_{\theta_\beta}\rangle$ when the line source is near the wall ($y_s/h = 0.17$). The general form of the profiles is somewhat different from that with the centreline line source. In contrast with the DNS profiles, the experimental profiles increase near the upper limits of the range of temperature fluctuations. This increase also appears when the source is at the centreline but with a (relatively) smaller magnitude. Note that figure 31(d) has been plotted with different axis ranges due to large rare excursions in this part of the flow, where some measurements are outside the plume, and the others in its outer edges.

Kailasnath *et al.* (1993) investigated the conditional scalar dissipation rate in three

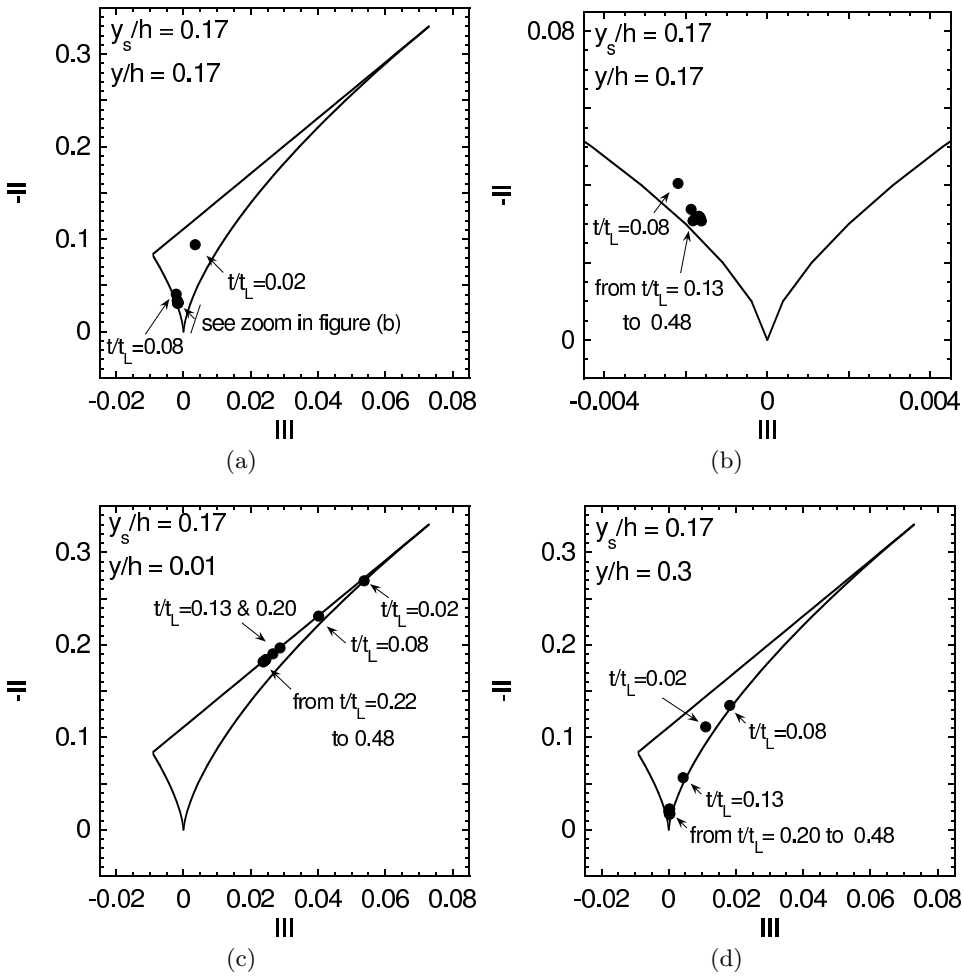

Figure 30: Anisotropy invariant map of ε_θ for $y_s/h = 0.17$ and $y/h = 0.17$ (a). A close-up of figure (a) is presented in figure (b). Anisotropy invariant map of ε_θ for $y_s/h = 0.17$ and $y/h = 0.01$ (c) and for $y_s/h = 0.17$ and $y/h = 0.3$ (d). Statistics were computed from $t/t_L = 0.02$ to 0.48.

different shear flows: wakes, jets, and in the atmospheric surface layer. They also found that the "hot side" of the conditional expectation $\langle \varepsilon_\theta | \theta \rangle$ increased with θ. They concluded that the very hot events associated with very high intermittent dissipation rates were non-universal. In addition, they mentioned that the low temperature events may also be non-universal but their contribution to the conditional expectation is small because the dissipation in the cold fluid is small. These observations are consistent with the present results.

Independently of the source location, figure 31 shows a tendency to isotropic behavior as the downstream distance from the source increases. At low θ/θ_{rms}, the experiments and DNSs agree relatively well. However, the discrepancies at large θ/θ_{rms} may be due to the fact that the large positive fluctuations of θ are rare and may suffer from a reduced level of statistical convergence.

The expectations of the components of the dissipation conditioned upon individual

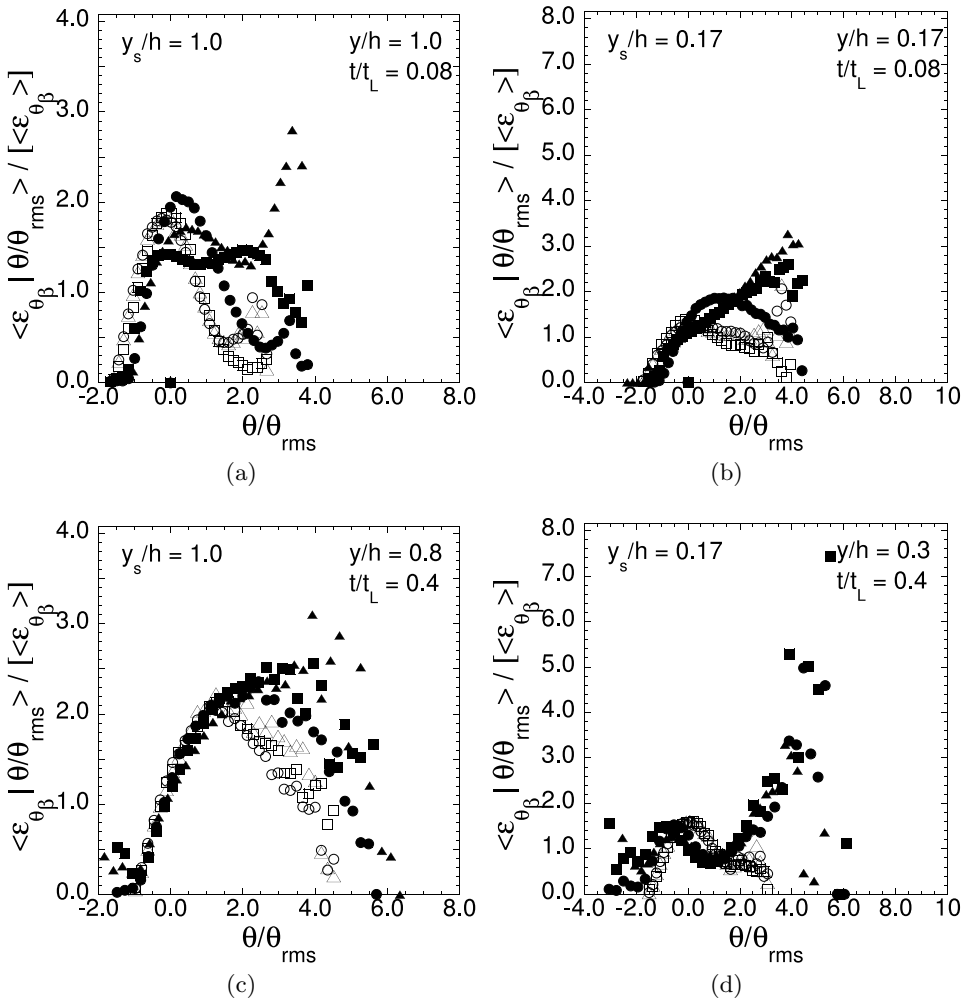

Figure 31: The expectation of the components of the temperature dissipation conditioned on the temperature fluctuations for $y_s/h = 1.0$ and $y_s/h = 0.17$ at two downstream locations: $t/t_L = 0.08$ (a, b) and $t/t_L = 0.4$ (c, d) at four wall-normal locations: $y/h = 1.0$ (a), $y/h = 0.17$ (b), $y/h = 0.8$ (c) and $y/h = 0.3$ (d). Experimental results are denoted by the solid symbols: $\langle \varepsilon_{\theta_x} | \theta \rangle$ (•), $\langle \varepsilon_{\theta_y} | \theta \rangle$ (■) and $\langle \varepsilon_{\theta_z} | \theta \rangle$ (▲) and the numerical results are denoted by the open symbols: $\langle \varepsilon_{\theta_x} | \theta \rangle$ (○), $\langle \varepsilon_{\theta_y} | \theta \rangle$ (□) and $\langle \varepsilon_{\theta_z} | \theta \rangle$ (△).

values of the temperature derivatives, $\langle \varepsilon_{\theta_\beta} | \partial\theta/\partial x \rangle$, where $\beta = x,\ y$ or z, are plotted in figure 32 for the two line source locations presented herein. These figures show that larger magnitudes of $\partial\theta/\partial x$ lead to higher values of ε_{θ_x} consistent with the definition $\varepsilon_{\theta_x} \equiv \alpha \langle (\partial\theta/\partial x)^2 \rangle$. In addition, ε_{θ_y} and ε_{θ_z} do not directly depend on $\partial\theta/\partial x$ which explains the flatter profiles obtained for $\langle \varepsilon_{\theta_y} | \partial\theta/\partial x \rangle$ and $\langle \varepsilon_{\theta_z} | \partial\theta/\partial x \rangle$. That being said, they are clearly not independent, especially farther downstream. Overall, a good agreement between experiments and DNSs is observed.

Figure 33 and 34 compare the expectations of $\varepsilon_{\theta_\beta}$ conditioned upon individual values of $\partial\theta/\partial x$, $\partial\theta/\partial y$, and $\partial\theta/\partial z$. The figures show consistent results for all three compo-

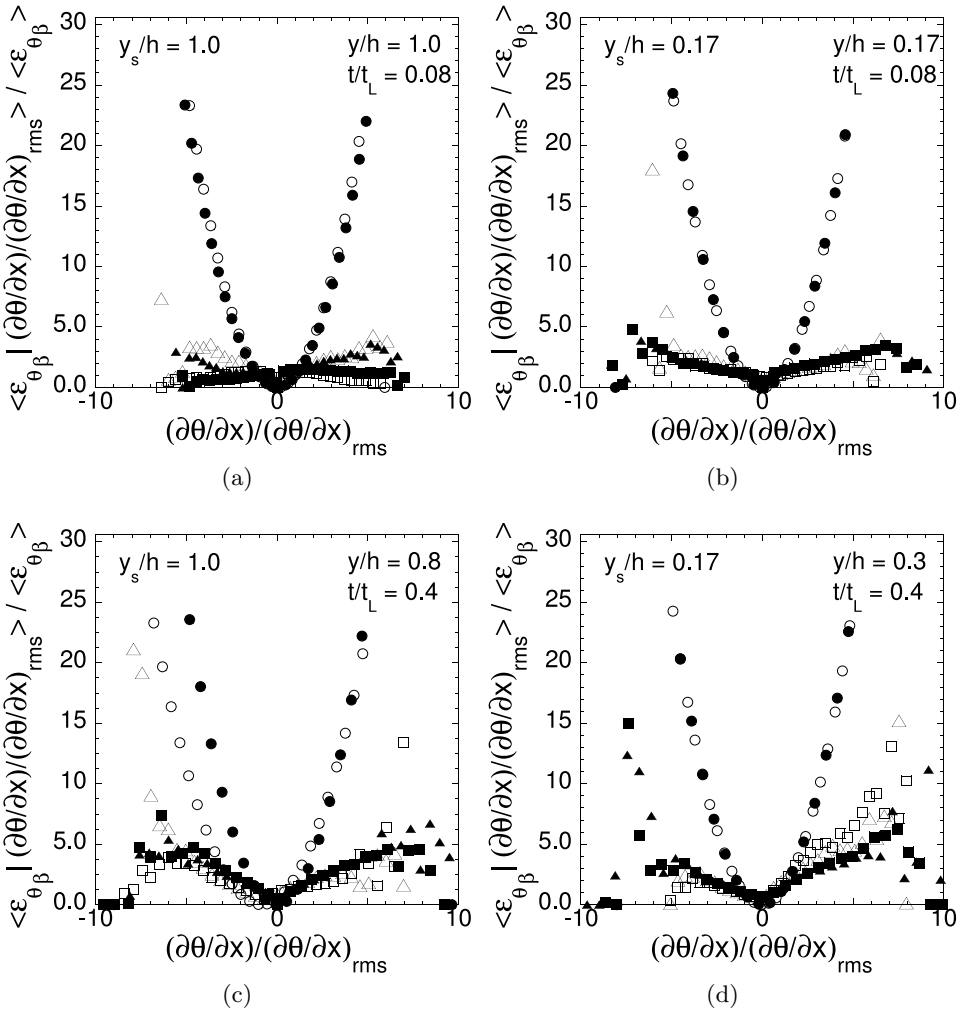

Figure 32: The expectation of the components of the temperature dissipation conditioned on the x-partial derivative of the temperature fluctuations for $y_s/h = 1.0$ and $y_s/h = 0.17$ at two downstream locations: $t/t_L = 0.08$ (a, b) and $t/t_L = 0.4$ (c, d) at four wall-normal locations: $y/h = 1.0$ (a), $y/h = 0.17$ (b), $y/h = 0.8$ (c) and $y/h = 0.3$ (d). Experimental results are denoted by the solid symbols: $\langle \varepsilon_{\theta_x} | \partial\theta/\partial x \rangle$ (•), $\langle \varepsilon_{\theta_y} | \partial\theta/\partial x \rangle$ (■) and $\langle \varepsilon_{\theta_z} | \partial\theta/\partial x \rangle$ (▲) and the numerical results are denoted by the open symbols: $\langle \varepsilon_{\theta_x} | \partial\theta/\partial x \rangle$ (○), $\langle \varepsilon_{\theta_y} | \partial\theta/\partial x \rangle$ (□) and $\langle \varepsilon_{\theta_z} | \partial\theta/\partial x \rangle$ (△).

nents, where *i*) the correlation is highest when considering the component of ε_θ and the derivative of θ measured in the same direction, and *ii*) a reduced, but clearly non-zero, correlation is observed for the expectations conditioned on the temperature derivative in a different direction.

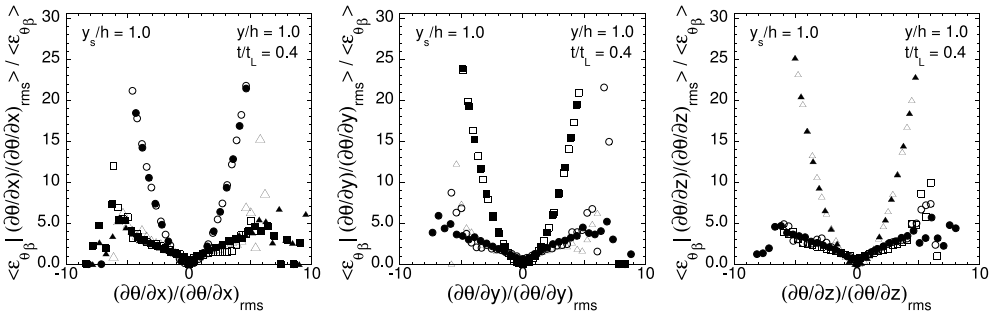

(a) (b) (c)

Figure 33: The expectation of the components of the temperature dissipation conditioned on the x-, y- and z-partial derivatives of the temperature fluctuations for $y_s/h = 1.0$ at $t/t_L = 0.4$ and $y/h = 1.0$. Experimental results are denoted by the solid symbols and the numerical results are denoted by the open symbols. (a) $\langle \varepsilon_{\theta_\beta} | \partial\theta/\partial x \rangle$. (b) $\langle \varepsilon_{\theta_\beta} | \partial\theta/\partial y \rangle$. (c) $\langle \varepsilon_{\theta_\beta} | \partial\theta/\partial z \rangle$. $\beta = x$ (circles); $\beta = y$ (squares);$\beta = z$ (triangles).

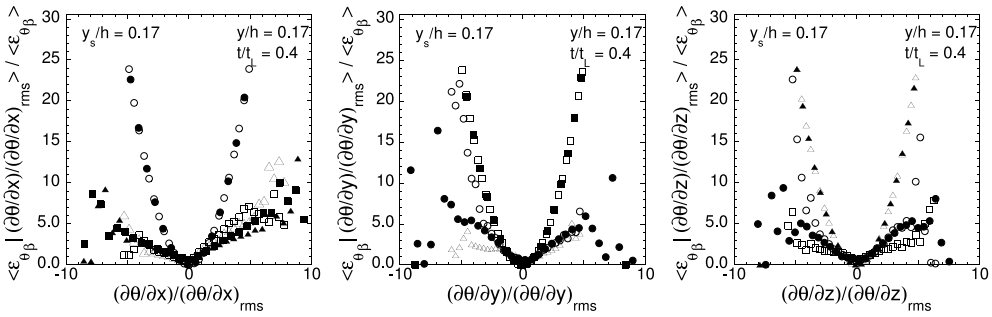

(a) (b) (c)

Figure 34: The expectation of the components of the temperature dissipation conditioned on the x-, y- and z-partial derivatives of the temperature fluctuations for $y_s/h = 0.17$ at $t/t_L = 0.4$ and $y/h = 0.17$. Experimental results are denoted by the solid symbols and the numerical results are denoted by the open symbols. (a) $\langle \varepsilon_{\theta_\beta} | \partial\theta/\partial x \rangle$. (b) $\langle \varepsilon_{\theta_\beta} | \partial\theta/\partial y \rangle$. (c) $\langle \varepsilon_{\theta_\beta} | \partial\theta/\partial z \rangle$. $\beta = x$ (circles); $\beta = y$ (squares);$\beta = z$ (triangles).

8. Conclusions

In the present work, the dissipation rate of a scalar (temperature) emitted from a concentrated line source in a fully developed turbulent channel flow was studied by means of both experiments *and* numerical simulations. The aim was to investigate the evolution of the small scales of the scalar field by measuring the (three components of the) scalar dissipation rate, ε_θ, at several downstream and wall-normal locations. The scalar was injected in a highly anisotropic manner and an examination of the downstream evolution of ε_θ permitted an investigation of the return to isotropy of the small scales of the scalar field.

Large- and small-scale statistics of the scalar field were reported for two different source locations ($y_s/h = 1.0$ and 0.17), with an emphasis on the small-scale ones, given the nature of this study. Overall, a good agreement between the experimental and numerical

data was obtained, confirming that the DNS is capable of resolving the experimentally measured dissipative scales. Some discrepancies between the two were, however, observed. These were attributed to the differences in the Reynolds number between the experiments ($Re_\tau = 520$) and the DNSs ($Re_\tau = 190$).

The principal contribution of this work is a detailed description of the downstream and transverse evolutions of small-scale statistics of the scalar field (with an emphasis on the scalar dissipation rate), as well as their dependence on the source location. The effect of the source location is a critical aspect of the present work, as it is an essential parameter that is only present in inhomogeneous flows – a category into which all practical flows fall. The present work provides insight into the effect of source location on the small-scale statistics of the scalar field, which, until now, had not been explicitly studied.

To this end, the downstream and transverse evolutions of the spectra and PDFs of the scalar gradients ($\partial\theta/\partial x_\beta$), ε_{θ_x}, ε_{θ_y}, ε_{θ_z} and ε_θ, as well as their dependence on source location, were analyzed. For the case of the centreline source, a tendency for these statistics to return to isotropy was always observed. When the source was located near the wall, the tendency to return to isotropy was not as evident, given that the production of ε_{θ_y} due to the mean velocity gradient, which was most evident in plots of $\varepsilon_{\theta_\beta}/\varepsilon_{\theta_\gamma}$, may be non-negligible at lower Reynolds numbers, such as those which characterized our numerical simulations. Because the near-wall region has characteristics that both reduce anisotropy (e.g. higher degrees of mixing, due to the more intense nature of the turbulence therein) and increase anisotropy (e.g. production of ε_{θ_y} by mean velocity gradients), the dependence of the return to isotropy on source location is complex, in addition to possibly being dependent on the Reynolds number, the Schmidt number (Yeung *et al.* 2002; Brethouwer *et al.* 2003, e.g.), etc. We have also argued that when the production of ε_{θ_y} by mean velocity gradients is non-negligible, a return to isotropy is inhibited by this mechanism, which possibly maintains the thermal time-scale at fixed value, unlike what was observed when small-scale isotropy of the scalar field was recovered. The return to isotropy of the scalar field was also quantified using anisotropy invariant maps for the scalar dissipation rate, which highlighted, downstream of the centreline source, i) the axisymmetric nature of scalar dissipation rate, and ii) an improved tendency towards isotropy of the small scales. The nature of the anisotropy invariant maps was, however, distinctly different in the near-wall region, varying from a one-dimensional state very close to the wall, towards an axisymmetric state as the centreline was approached. Lastly, conditional expectations of the three components of ε_θ were presented, which, in addition to providing insight into the scalar field's structure, should be of benefit to those developing mixing models for PDF methods.

The more rapid return to isotropy of certain statistics (e.g. both the spectra and PDFs of the scalar gradients, PDFs of ε_θ, etc.) in the near-wall region are consistent with the scalar field undergoing increased mixing in regions of more intense turbulence (i.e. regions of locally higher turbulent Reynolds numbers). However, in the current flow, the increased values of u_{rms} are associated with the larger contribution of production of turbulent kinetic energy by mean velocity gradients, which as previously noted, also serves to produce anisotropy. Increased mixing in regions or more intense turbulence is consistent with the arguments of Rosset *et al.* (2001) and Gonzalez & Paranthoën (2003), as increased levels of turbulence can be associated with increased vorticity. Rosset *et al.* (2001) hypothesized that the return to isotropy in a flow in which the scalar field is injected at small scales is caused by both molecular dissipation and stretching, in which the latter is effected by both strain and rotation, with rotation serving to reorient the scalar gradients and thus "isotropizing" the scalar field. Gonzalez & Paranthoën (2003) further analyzed the work of Rosset *et al.* (2001) and suggested that the return

to isotropy was "governed by vorticity at scales of the order of the instantaneous scalar sheet thickness," arguing that vorticity at smaller scales could not significantly distort the plume, whereas that at large scales would be able to rotate the plume, but would be weaker (assuming typical Kolmogorov arguments for the dependence of vorticity on length scale).

In addition to the above, it is worth reiterating the comments of Rosset *et al.* (2001) and Gonzalez & Paranthoën (2003), who emphasize that flows in which the scalar is injected at small scales are notably different from those in which the scalar is injected at large-scales (i.e., by way of a mean scalar gradient). In the latter class of flows, anisotropy is continually generated by the large-scale anisotropic injection mechanism. In the current case of small-scale injection by a line (or point) source, the small-scale anisotropy does not originate from large-scale anisotropy being transferred to smaller scales, because it originates at small scales, and the mean scalar gradients, which are the source of the anisotropy, become smaller and smaller as the plume is increasingly well mixed, thus also promoting, in part, a return to isotropy. Nevertheless, the exact nature of the return to isotropy of a scalar field injected at small scales merits additional investigations, such as i) ones that might focus on the effect of the intensity of the turbulence / local Reynolds number, without compounding the results with a change in the mean velocity gradient / production of turbulent kinetic energy, ii) further investigating the effect of Schmidt number, or ii) numerical simulations in which simultaneous, small-scale velocity and scalar statistics could be recorded, because experimentally measuring all three scalar gradients and all nine velocity ones remains an exceedingly difficult task.

9. Acknowledgements

The authors acknowledge the gracious support of the Natural Sciences and Engineering Research Council of Canada.

REFERENCES

Abe, H., Kawamura, H. & Matsuo, Y. 2001 Direct numerical simulation of a fully developed turbulent channel flow with respect to the Reynolds number dependence. *J. Fluids Eng.* **123**, 382–393.

Abe, H., Kawamura, H. & Matsuo, Y. 2004 Surface heat-flux fluctuations in a turbulent channel flow up to $Re_\tau = 1020$ with $Pr = 0.025$ and 0.71. *Int. J. Heat Fluid Flow* **25**, 404–419.

Anselmet, F., Djeridi, H. & Fulachier, L. 1994 Joint statistics of a passive scalar and its dissipation in turbulent flows. *J. Fluid Mech.* **280**, 173–197.

Anselmet, F., Djeridi, H. & Fulachier, L. 1997 Simultaneous measurements of temperature and its dissipation using pairs of parallel cold wires. *Exp. Fluids* **23**, 177–186.

Antonia, R. A. & Browne, L. W. B. 1986 Anisotropy of the temperature dissipation in a turbulent wake. *J. Fluid Mech.* **163**, 393–403.

Antonia, R. A. & Kim, J. 1994 A numerical study of local isotropy of turbulence. *Phys. Fluids* **6**, 834–841.

Antonia, R. A., Kim, J. & Browne, L. W. B. 1991 Some characteristics of small-scale turbulence in a turbulent duct flow. *J. Fluid Mech.* **233**, 369–388.

Antonia, R. A. & Mi, J. 1993 Temperature dissipation in a turbulent round jet. *J. Fluid Mech.* **250**, 531–551.

Bakosi, J., Franzese, P. & Boybeyi, Z. 2007 Probability density function modeling of scalar mixing from concentrated sources in turbulent channel flow. *Phys. Fluids* **19**, 115106.

Balsara, D. S. 2001 Divergence-free adaptive mesh refinement for magnetohydrodynamics. *J. Comput. Phys.* **174**, 614–648.

Boppana, V. B. L., Xie, Z. T. & Castro, I. P. 2012 Large-eddy simulation of dispersion from line sources in a turbulent channel flow. *Flow Turbul. Combust.* **88**, 311–342.

Brethouwer, G., Boersma, B. J., Pourquie, M. & Nieuwstadt, F. T. M. 1999 Direct numerical simulation of turbulent mixing of a passive scalar in pipe flow. *Eur. J. Mech. B-Fluid.* **18**, 739–756.

Brethouwer, G., Hunt, J. C. R. & Nieuwstadt, F. T. M. 2003 Micro-structure and lagrangian statistics of the scalar field with a mean gradient in isotropic turbulence. *J. Fluid Mech.* **474**, 193–225.

Chamecki, M., Meneveau, C. & Parlange, M. B. 2008 A hybrid spectral/finite-volume algorithm for large-eddy simulation of scalars in the atmospheric boundary layer. *Bound.-Lay. Meteorol.* **128**, 473–484.

Chung, M. K. & Kyong, N. H. 1989 Measurement of turbulent dispersion behind a fine cylindrical heat source in a weakly sheared flow. *J. Fluid Mech.* **205**, 171–193.

Clyne, J., Mininni, P., Norton, A. & Rast, M. 2007 Interactive desktop analysis of high resolution simulations: application to turbulent plume dynamics and current sheet formation. *New J. Phys.* **9**, 301.

Clyne, J. & Rast, M. 2005 A prototype discovery environment for analyzing and visualizing terascale turbulent fluid flow simulations. In *EProceedings of Visualization and Data Analysis 2005*, pp. 284–294.

Corrsin, S. 1951 On the spectrum of isotropic temperature fluctuations in an isotropic turbulence. *J. Appl. Phys.* **22**, 469–473.

Corrsin, S. 1952 Heat transfer in isotropic turbulence. *J. Appl. Phys.* **23**, 113–118.

Corrsin, S. 1953 Remarks on turbulent heat transfer. *Proceedings of the Iowa Thermodynamics Symposium, State University of Iowa, Iowa City,* pp. 5–30.

Costa-Patry, E. & Mydlarski, L. 2008 Mixing of two thermal fields emitted from line sources in turbulent channel flow. *J. Fluid Mech.* **609**, 349–375.

Dahm, W. J. A. & Buch, K. A. 1989 Lognormality of the scalar dissipation pdf in turbulent flows. *Phys. Fluids A-Fluid* **1**, 1290–1293.

Danaila, L., Antonia, R. A. & Burattini, P. 2012 Comparison between kinetic energy and passive scalar energy transfer in locally homogeneous isotropic turbulence. *Physica D: Nonlinear Phenomena* **241**, 224–231.

Danaila, L., Zhou, T., Anselmet, F. & Antonia, R. A. 2000 Calibration of a temperature dissipation probe in decaying grid turbulence. *Exp. Fluids* **28**, 45–50.

Donzis, D. A., Sreenivasan, K. R. & Yeung, P. K. 2005 Scalar dissipation rate and dissipative anomaly in isotropic turbulence. *J. Fluid Mech* **532**, 199–216.

Fackrell, J. E. & Robins, A. G. 1982 Concentration fluctuations and fluxes in plumes from point sources in a turbulent boundary layer. *J. Fluid Mech.* **117**, 1–26.

Galantucci, L. & Quadrio, M. 2010 Very fine near-wall structures in turbulent scalar mixing. *Int. J. Heat Fluid Flow* **31**, 499–506.

Germaine, E., Mydlarski, L. & Cortelezzi, L. 2013 3DFLUX: A high-order fully three-dimensional flux integral solver for the scalar transport equation. *J. Comput. Phys.* **240**, 121–144.

Gibson, J. F. 2010 Channelflow: A spectral Navier-Stokes simulator in `C++`. *Tech. Rep.*. University of New Hampshire.

Gibson, J. F., Halcrow, J. & Cvitanović, P. 2008 Visualizing the geometry of state space in plane Couette flow. *J. Fluid Mech.* **611**, 107–130.

Gonzalez, M. 2000 Study of the anisotropy of a passive scalar field at the level of dissipation. *Phys. Fluids* **12**, 2302–2310.

Gonzalez, M. & Paranthoën, P. 2003 On the role of vorticity in the microstructure of a passive scalar field. *Phys. Fluids* **16**, 219–221.

Gurvich, A. S. & Yaglom, A. M. 1967 Breakdown of eddies and probability distributions for small-scale turbulence. *Phys. Fluids* **10**, S59–S65.

Holzer, M. & Siggia, E. D. 1994 Turbulent mixing of a passive scalar. *Phys. Fluids* **6**, 1820–1837.

Hussain, A. K. M. F. & Reynolds, W. C. 1975 Measurements in fully developed turbulent channel flow. *J. Fluids Eng.* **97**, 568–578.

Incropera, F. P., De Witt, D. P., Bergman, T. L. & Lavine, A. S. 2007 *Fundamentals of heat and mass transfer*, 6th edn. New York: John Wiley and Sons Inc.

Jayesh & Warhaft, Z. 1992 Probability distribution, conditional dissipation, and transport of passive temperature fluctuations in grid-generated turbulence. *Phys. Fluids A* **4**, 2292–2307.

Johansson, A. V. & Wikström, P. M. 1999 DNS and modelling of passive scalar transport in turbulent channel flow with a focus on scalar dissipation rate modelling. *Flow Turbul. Combust.* **63**, 223–245.

Kailasnath, P., Sreenivasan, K. R. & Saylor, J. R. 1993 Conditional scalar dissipation rates in turbulent wakes, jets, and boundary layers. *Phys. Fluids A* **5**, 3207–3215.

Karnik, U. & Tavoularis, S. 1989 Measurements of heat diffusion from a continuous line source in a uniformly sheared turbulent flow. *J. Fluid Mech.* **202**, 233–261.

Kawamura, H., Ohsaka, K., Abe, H. & Yamamoto, K. 1998 DNS of turbulent heat transfer in channel flow with low to medium-high prandtl number fluid. *Int. J. Heat Fluid Fl.* **19**, 482–491.

Kim, J., Moin, P. & Moser, R. 1987 Turbulence statistics in fully developed channel flow at low Reynolds number. *J. Fluid Mech.* **177**, 133–166.

Kolmogorov, A. 1941 The local structure of turbulence in incompressible viscous fluid for very large Reynolds numbers. *Dokl. Akad. Nauk SSSR* **30**, 301–305.

Kozuka, M., Seki, Y. & Kawamura, H. 2009 DNS of turbulent heat transfer in a channel flow with a high spatial resolution. *Int. J. Heat Fluid Fl.* **30**, 514–524.

LaRue, J. C. & Libby, P. A. 1981 Thermal mixing layer downstream of half-heated turbulence grid. *Phys. Fluids* **24**, 597–603.

Lavertu, R. A. & Mydlarski, L. 2005 Scalar mixing from a concentrated source in turbulent channel flow. *J. Fluid Mech.* **528**, 135–172.

Lemay, J. & Benaïssa, A. 2001 Improvement of cold-wire response for measurement of temperature dissipation. *Exp. Fluids* **31**, 347–356.

Lepore, J. & Mydlarski, L. 2011 Lateral dispersion from a concentrated line source in turbulent channel flow. *J. Fluid Mech.* **678**, 417–450.

Li, S. & Li, H. 2004 A novel approach of divergence-free reconstruction for adaptive mesh refinement. *J. Comput. Phys.* **199**, 1–15.

Livescu, D., Jaberi, F. A. & Madnia, C. K. 2000 Passive-scalar wake behind a line source in grid turbulence. *J. Fluid Mech.* **416**, 117–149.

Lockwood, F. C. & Moneib, H. A. 1980 Fluctuating temperature measurements in a heated round free jet. *Combust. Sci. Technol.* **22**, 63–81.

Lumley, J. L. 1978 Computational modeling of turbulent flows. *Adv. Appl. Mech.* **18**, 123–176.

Ma, B. K. & Warhaft, Z. 1986 Some aspects of the thermal mixing layer in grid turbulence. *Phys. Fluids* **29**, 3114–3120.

Moin, P. & Mahesh, K. 1998 Direct numerical simulation: a tool in turbulence research. *Annu. Rev. Fluid Mech.* **30**, 539–578.

Moser, R. D., Kim, J. & Mansour, N. N. 1999 Direct numerical simulation of turbulent channel flow up to $Re = 590$. *Phys. Fluids* **11**, 943–945.

Mydlarski, L. 2003 Mixed velocity-passive scalar statistics in high-Reynolds-number turbulence. *J. Fluid Mech.* **475**, 173–203.

Mydlarski, L., Danaila, L. & Lavertu, R. A. 2007 Isotropy of the temperature field downstream of a line source in turbulent channel flow. *Advances in Turbulence XI, Proc. the 11th EUROMECH European Turbulence Conference* **117**, 500–502.

Obukhov, AM 1949 Structure of the temperature field in a turbulent current. *Izv. Aka. Nauk. SSSR, Ser. Geograf. Geofiz* **13**, 58–69.

Paranthoën, P., Fouari, A., Dupont, A. & Lecordier, J. C. 1988 Dispersion measurements in turbulent flows (boundary layer and plane jet). *Int. J. Heat Mass Transfer* **31**, 153–165.

Pope, S. B. & Ching, E. S. C. 1993 Stationary probability density functions: An exact result. *Phys. Fluids* **5**, 1529–1531.

Prasad, R. R. & Sreenivasan, K. R. 1990 Quantitative three-dimensional imaging and the structure of passive scalar fields in fully turbulent flows. *J. Fluid Mech.* **216**, 1–34.

Raupach, M. R. & Legg, B. J. 1983 Turbulent dispersion from an elevated line source: measurements of wind-concentration moments and budgets. *J. Fluid Mech.* **136**, 111–137.

Rosset, L., Paranthoën, P., Lecordier, J. C. & Gonzalez, M. 2001 Anisotropy of a thermal field at dissipative scales in the case of small-scale injection. *Phys. Fluids* **13**, 3729–3737.

Schumacher, J. & Sreenivasan, K. R. 2005 Statistics and geometry of passive scalars in turbulence. *Phys. Fluids* **17**, 1–9.

Schumacher, J., Sreenivasan, K. R. & Yeung, P. K. 2005 Very fine structures in scalar mixing. *J. Fluid Mech.* **531**, 113–122.

Schwertfirm, F. & Manhart, M. 2007 DNS of passive scalar transport in turbulent channel flow at high Schmidt numbers. *Int. J. Heat Fluid Fl.* **28**, 1204–1214.

Simens, M. P., Jiménez, J., Hoyas, S. & Mizuno, Y. 2009 A high-resolution code for turbulent boundary layers. *J. Comput. Phys.* **228**, 4218–4231.

Sinai, Y. G. & Yakhot, V. 1989 Limiting probability distributions of a passive scalar in a random velocity field. *Phys. Rev. Lett.* **63**, 1962–1964.

Sreenivasan, K. R. 1984 On the scaling of the turbulence energy dissipation rate. *Phys. Fluids* **27**, 1048–1051.

Sreenivasan, K. R. 1991 On local isotropy of passive scalars in turbulent shear flows. *Proc. R. Soc. London, Ser. A* **434**, 165–182.

Sreenivasan, K. R., Antonia, R. A. & Danh, H. Q. 1977 Temperature dissipation fluctuations in a turbulent boundary layer. *Phys. Fluids* **20**, 1238–1249.

Stapountzis, H., Sawford, B. L., Hunt, J. C. R. & Britter, R. E. 1986 Structure of the temperature field downwind of a line source in grid turbulence. *J. Fluid Mech.* **165**, 401–424.

Su, L. K. & Clemens, N. T. 2003 The structure of fine-scale scalar mixing in gas-phase planar turbulent jets. *J. Fluid Mech.* **488**, 1–29.

Sutton, J. A. & Driscoll, J. F. 2013 Measurements and statistics of mixture fraction and scalar dissipation rates in turbulent non-premixed jet flames. *Combust. Flame* **160**, 1767–1778.

Taylor, G. I. 1935 Statistical theory of turbulence. parts $1-4$. *Proc. R. Soc. London, Ser. A* **151**, 421–478.

Tennekes, H. & Lumley, J. L. 1972 *A first course in turbulence*. Cambridge, MA: MIT press.

Thomson, D. J. 1996 The second-order moment structure of dispersing plumes and puffs. *J. Fluid Mech.* **320**, 305–329.

Thoroddsen, S. T. & Van Atta, C. W. 1996 Experiments on density-gradient anisotropies and scalar dissipation of turbulence in a stably stratified fluid. *J. Fluid Mech.* **322**, 383–409.

Tong, C. & Warhaft, Z. 1995 Passive scalar dispersion and mixing in a turbulent jet. *J. Fluid Mech* **292**, 1–38.

Uberoi, M. S. & Corrsin, S. 1952 Diffusion of heat from a line source in isotropic turbulence. *Tech. Rep.*. Nat. Adv. Comm. Aero.

Van Atta, C. 1991 Local isotropy of the smallest scales of turbulent scalar and velocity fields. *Proc. R. Soc. London, Ser. A* **434**, 139–147.

Vrieling, A. J. & Nieuwstadt, F. T. M. 2003 Turbulent dispersion from nearby point sources interference of the concentration statistics. *Atmos. Environ.* **37**, 4493–4506.

Warhaft, Z. 1984 The interference of thermal fields from line sources in grid turbulence. *J. Fluid Mech.* **144**, 363–387.

Warhaft, Z. 2000 Passive scalars in turbulent flows. *Annu. Rev. Fluid Mech.* **32**, 203–240.

Wyngaard, J. C. 1969 Spatial resolution of the vorticity meter and other hot-wire arrays. *J. Phys. E: Sci. Instrum.* **2**, 983–987.

Yeung, P. K., Xu, S. & Sreenivasan, K. R. 2002 Schmidt number effects on turbulent transport with uniform mean scalar gradient. *Phys. Fluids* **14**, 4178–4191.

Zhou, T., Antonia, R. A., Lasserre, J. J., Coantic, M. & Anselmet, F. 2003 Transverse velocity and temperature derivative measurements in grid turbulence. *Exp. Fluids* **34**, 449–459.